The Oxo-Wall Remains Intact: A Tetrahedrally Distorted Co(IV)-Oxo Complex

Jindou Yang,[a,†] Hai T. Dong,[b,†] Mi Sook Seo,[a] Virginia A. Larson,[b] Yong-Min Lee,[a] Jason Shearer,[c*] Nicolai Lehnert,[b*] and Wonwoo Nam[a,d*]

[a] *Department of Chemistry and Nano Science, Ewha Womans University, Seoul 03760, Korea*

[b] *Department of Chemistry and Department of Biophysics, University of Michigan, Ann Arbor, MI 48109-1055, USA.*

[c] *Department of Chemistry, Trinity University, San Antonio, TX 78212-7200, USA*

[d] *School of Chemistry and Chemical Engineering, University of Jinan, Jinan 250022, China*

ABSTRACT

In this paper, we report the preparation, spectroscopic and theoretical characterization, and reactivity studies of a Co(IV)-oxo complex bearing an N4-macrocyclic co-ligand 12-TBC (12-TBC = 1,4,7,10-tetrabenzyl-1,4,7,10-tetraazacyclododecane). Based on the ligand and the structure of the Co(II) precursor, $[Co^{II}(12\text{-}TBC)(CF_3SO_3)_2]$, one would assume that this species corresponds to a tetragonal Co(IV)-oxo complex, but the spectroscopic data do not support this notion. Co K-edge XAS data show that the treatment of the Co(II) precursor with iodosylbenzene (PhIO) as an oxidant at –40 °C in the presence of a proton source leads to a distinct shift in the Co K-edge, in agreement with the formation of a Co(IV) intermediate. The presence of the oxo group is further demonstrated by resonance Raman (rRaman) spectroscopy. Interestingly, the EPR data of this complex show a high degree of rhombicity, indicating structural distortion. This is further supported by the EXAFS data. Using DFT calculations, a structural model is developed for this complex with a ligand-protonated structure that features a Co=O---HN hydrogen bond and a four-coordinate Co center in a seesaw-shaped coordination geometry. Magnetic circular dichroism (MCD) spectroscopy further supports this finding. The hydrogen bond leads to an interesting polarization of the Co-oxo π-bonds, where one O(p) lone-pair is stabilized and leads to a regular Co(d) interaction, whereas the other π-bond shows an inverted ligand field. The reactivity of this complex in hydrogen atom and oxygen atom transfer reactions is discussed as well.

1. Introduction

High-valent metal-oxo species are of great interest as short-lived highly reactive intermediates in important biological processes and chemical transformations.[1-11] Notable reactions that involve metal-oxo complexes include the O-O bond formation step for water oxidation in Photosystem II[12-16] and reactive intermediates in heme and nonheme iron oxygenases.[10, 17, 18] While ingenious studies of these systems have provided important information on the geometric and electronic structure, function, and reactivity of these species, much is still unknown. Since these metal-oxo moieties in Nature are too short-lived to be fully characterized, chemists have synthesized model complexes to further investigate their bonding and reactivity and establish structure/function correlations for these species.[3, 19, 20] Synthetic chemists have also expanded beyond Nature's iron and manganese complexes to other transition metals.[7, 10, 11, 21-23] High-valent cobalt-oxo species are particularly relevant for their proposed role in artificial water oxidation and their ability to function in oxygen atom transfer (OAT) and hydrogen atom transfer (HAT) reactions.[24-28]

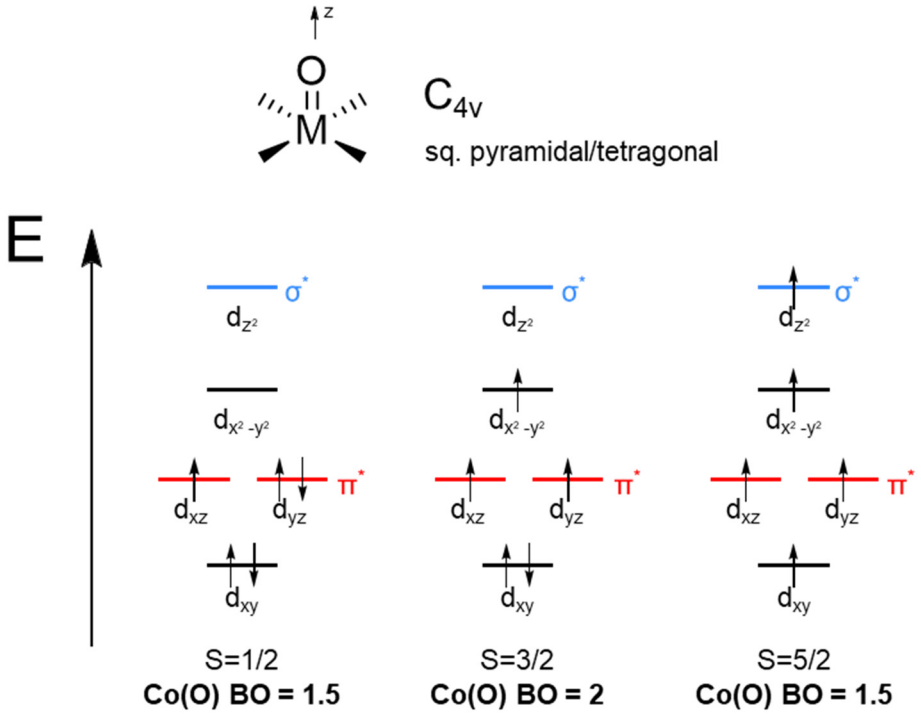

Scheme 1. d-Orbital splitting diagrams for square pyramidal/tetragonal cobalt(IV)-oxo complexes, illustrating how different spin states cause different Co-oxo formal bond orders as the electrons fill orbitals that are non-bonding (black), π-antibonding (red), or σ-antibonding (blue) with respect to the Co-oxo bond.

While quite a number of early first row transition metal-oxo complexes have been prepared and characterized, examples of the later first row transition metals, such as cobalt and beyond, are rare. The reason why these are so challenging to observe is their electronic instability, known as the oxo wall.[29] This and recent advances in the field are described in more detail in a recent review by some of us.[30] In brief, a terminal metal oxygen bond is destabilized for transition metal-oxo complexes of groups 9, 10, and 11 with tetragonal symmetry, because the d-electrons populate the metal-oxo π-antibonding orbitals, lowering the metal-oxo bond order (see Scheme 1). This increases the reactivity of the metal-oxo unit and makes it more prone to protonation or formation of oxo-bridged clusters. In addition, the bonding orbitals are increasingly localized on the high-valent metal ion, giving the complex more of a metal-oxyl character. This reduction in the metal-oxo bond order and the oxygen Lewis basicity lead to highly reactive complexes. However, changing the spin state or geometry of the complex can allow for a circumvention (or even breaking) of the oxo wall,[30] and formation of moderately stable metal-oxo complexes for these later transition metals.

Previously, only a few spectroscopically well-characterized terminal metal-oxo complexes past the oxo wall have been reported.[30] Early examples employed heavy metals, such as a trigonal-bipyramidal iridium complex[31] and a square-planar platinum complex.[32] These complexes are challenging to study; a few different heavy metal-oxo complexes were thought to break the oxo wall, but their structures were later revised.[33]

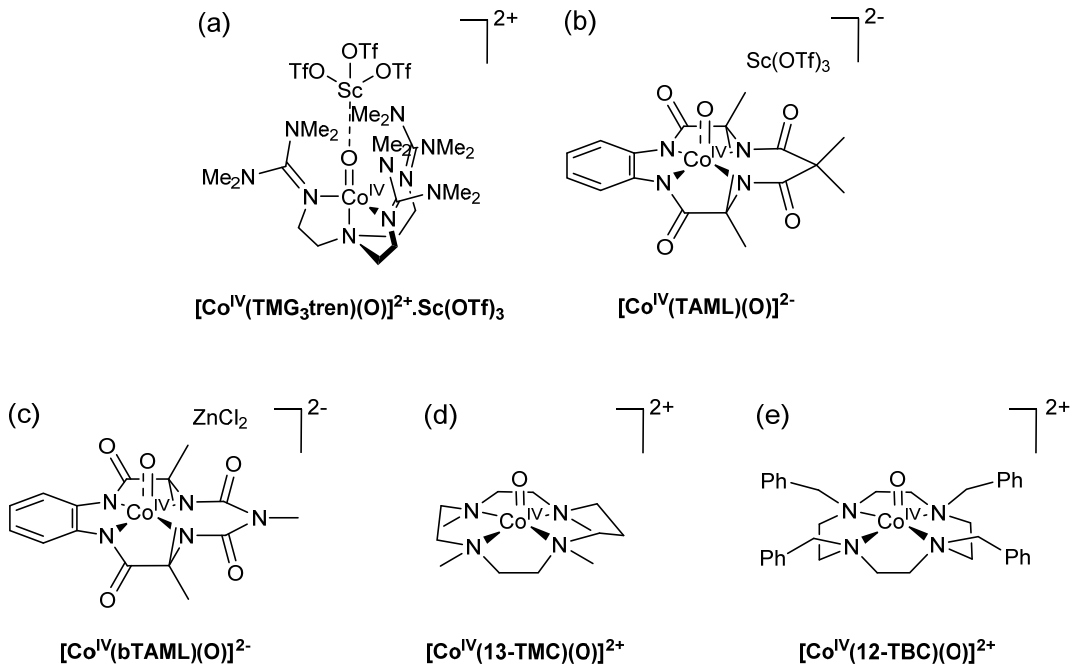

Figure 1. Proposed structures of Co(IV)-oxo complexes reported previously (a – d) and the new Co(IV)-oxo complex reported here (e).

While terminal Co-oxo complexes are rare, they have been supported as active intermediates in several reactions, and in recent years a few complexes stable enough for spectroscopic characterization have been prepared, for example by Anderson and coworkers.[34,35] In addition, high-valent Co-oxo complexes have been hypothesized in C-H activation[36-38] and OAT reactions.[39,40] In 2011, $[Co(TMG_3tren)(O)]^{2+}$ (TMG_3tren = tris[2-(N-tetramethylguanidyl)ethyl]amine), stabilized by scandium triflate (Figure 1a), was reported by Ray and co-workers and characterized by electron paramagnetic resonance (EPR), X-ray absorption spectroscopy (XAS), extended X-ray absorption fine structure (EXAFS), and density functional theory (DFT) calculations.[41] This complex was shown by EPR to have an intermediate-spin (IS) S = 3/2 ground state, which supports a Co(IV)-O type species bridged to the Sc^{3+} ion. Later, Borovik and co-workers suggested that a hydroxide ligand actually bridges the cobalt and scandium center and that the complex contains a Co(III) center.[42] $[Co(TAML)(O)]^{2-}$ (TAML =

tetraamido macrocyclic ligand), also stabilized with scandium triflate, was reported in 2014 by Nam, Ray, and co-workers and characterized by EPR, UV-vis, XAS, and EXAFS (see Figure 1b).[43] However, since the $TAML^{4-}$ ligand is non-innocent, as demonstrated by Collins and co-workers (for example, [Co(IV)(TAML)] was identified as a Co(III)($TAML^{+\bullet}$) complex),[44, 45] questions remained with respect to the actual presence of a Co(IV) center in this complex. The corresponding biuret-modified complex reported by Sen Gupta and co-workers is stabilized by zinc chloride (see Figure 1c), and this species was characterized by electrochemistry and UV-vis spectroscopy, showing similarities to $[Co(TAML)(O)]^{2-}$.[46] Note that a Lewis acid (LA) can stabilize a metal-oxo unit in several ways. It can interact directly with the oxo ligand, sometimes changing the oxidation state of the metal.[47, 48] In other cases, the LA has been shown to interact with the co-ligand, stabilizing the metal-oxo unit by reducing the axial donation to the metal center.[49] While LAs are useful in modeling corresponding interactions in Photosystem II and have allowed for the first spectroscopic characterization of a Co(IV)-oxo species, synthetic chemists next tried to find such a complex without the presence of a LA, at least not coordinated to the metal-oxo unit.

In 2017, Nam and co-workers reported a Co(IV)-oxo complex, $[Co(13\text{-}TMC)(O)]^{2+}$ (13-TMC = 1,4,7,10-tetramethyl-1,4,7,10-tetraazacyclotridecane) (Figure 1d),[50] which is of particular relevance to this study as it constitutes by far the best characterized terminal high-valent Co(IV)-oxo complex to date. In addition, 13-TMC is very similar to the 12-TBC co-ligand (12-TBC = 1,4,7,10-tetrabenzyl-1,4,7,10-tetraazacyclododecane) used here; while 13-TMC has N-methyl substituents, this 12-TBC ligand has benzyl groups at the central nitrogen atoms of the (slightly smaller) N4-macrocycle. The Co-oxo complex $[Co(13\text{-}TMC)(O)]^{2+}$ has a $t_{1/2}$ of 3 h at –40 °C, and could therefore be characterized by UV-vis, resonance Raman (rRaman), EPR, XAS, EXAFS, and mass spectrometry (MS). From rRaman, MS, and EXAFS studies, the presence of a cobalt-oxo moiety in this complex was confirmed with a cobalt-oxo distance of 1.72 Å. EPR shows a complex with an IS S = 3/2 ground state, allowing a formal Co-O bond order of 2. Interestingly,

this species is only stable in the presence of a proton donor. This complex shows reactivity consistent with a metal-oxo species, including intermetal oxo transfer, C-H bond activation, and olefin epoxidation.

Herein, we describe the synthesis and characterization of a new Co-O complex, $[Co(12\text{-}TBC)(O)]^{2+}$, schematically shown in Figure 1e, which was prepared from the corresponding Co(II) precursor using iodosylbenzene (PhIO) at –40 °C. Several spectroscopic techniques, including UV-vis, rRaman, EPR, XAS, EXAFS, MS, and magnetic circular dichroism (MCD), were used to investigate this intermediate. DFT and CASSCF/NEVPT2 calculations were further used to corroborate these experimental studies. Our results constitute only the second report of a well-characterized, formally Co(IV)-oxo species. In addition, detailed analysis of the spectroscopic results shows an interesting tetrahedral distortion of the complex, caused by ligand protonation, which leads to a T-shaped coordination geometry about the Co center. This unexpected structure might be relevant for other Co-oxo complexes, such as those previously reported, especially $[Co(13\text{-}TMC)(O)]^{2+}$. With the symmetry of the complex being distorted from tetragonal symmetry, we conclude that the oxo wall still holds, despite the presence of a Co=O double bond. These results are discussed in this manuscript.

2. Results & Analysis

2.1 Synthesis and Basic Characterization of the Co(IV)-oxo Complex

The starting cobalt complex, $[Co^{II}(12\text{-}TBC)(CF_3SO_3)_2]$ (**1**), was synthesized and structurally and spectroscopically characterized (see Experimental Section; Supporting Information (SI), Tables S1 and S2 and Figures S1 and S2). Addition of PhIO as an oxidant to a solution of **1** in acetone/trifluoroethanol (TFE; *v/v* = 4:1) at –40 °C afforded the gradual change of the solution color from red to deep brown with λ_{max} = 720 nm (Figure 2a). The intermediate, denoted as **2**, was

metastable ($t_{1/2}$ ~2 h) at –40 °C, allowing us to characterize it with various spectroscopic techniques, such as UV-vis, cold spray time-of-flight mass spectrometry (CSI-MS), EPR, rRaman, MCD, and XAS/EXAFS (*vide infra*).

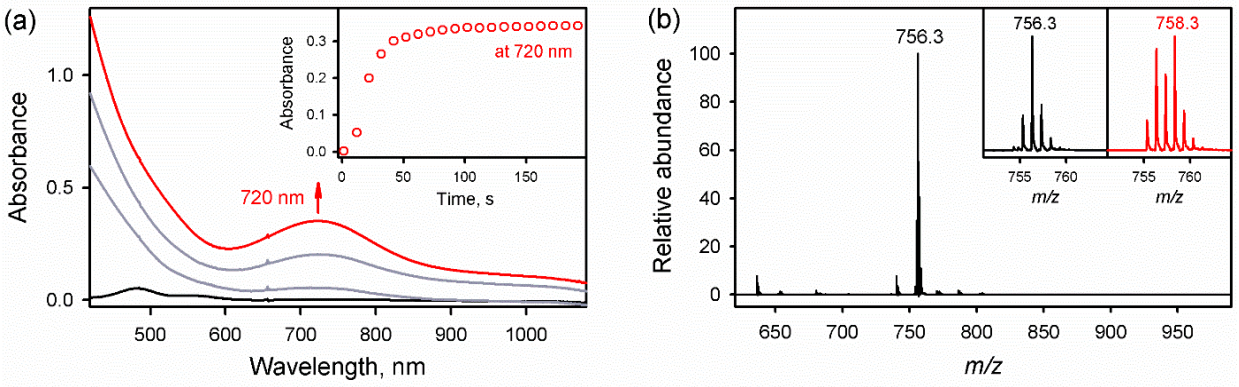

Figure 2. (a) UV-vis spectral changes observed upon addition of PhIO (3.5 equiv) to a solution of **1** (black line; 0.50 mM) in acetone/TFE (*v/v* = 4/1) at –40 °C. The inset shows the time course monitored at 720 nm due to the formation of **2**. (b) CSI-MS spectrum of **2**. Peak at *m/z* = 756.3 corresponds to [Co(12-TBC)(O)(CF_3SO_3)]$^+$ (calcd. *m/z* = 756.2). The insets show the observed isotope distribution patterns for **2**-^{16}O (left panel) and **2**-^{18}O (right panel).

The CSI-MS of **2** in positive mode shows a prominent ion peak at a mass-to-charge ratio (*m/z*) of 756.3, which corresponds to [Co(12-TBC)(O)(CF_3SO_3)]$^+$ (calcd. *m/z* of 756.2) (Figure 2b). When **2** was generated with isotopically labeled PhI^{18}O, a two-mass unit shift from *m/z* = 756.3 to 758.3 was observed (Figure 2b, inset, right panel), demonstrating that **2** contains an oxygen atom derived from PhIO. Following the synthesis of this molecule, a variety of characterization techniques were used to determine its geometric and electronic structure.

2.2. XAS and Structural Characterization by EXAFS

Compound **2** was analyzed by cobalt K-edge X-ray absorption spectroscopy. Figure 3 displays the XANES region of the cobalt K-edge X-ray absorption spectra of **1** and **2**. Compound **1**, which contains a formal Co(II) center, possesses a pre-edge feature at 7709.8(1) eV and an edge jump

at 7717.3(3) eV. Upon oxidation to **2**, the edge blue-shifts by 4.7(3) eV to 7722.0(3) eV indicating a change in oxidation state from Co(II) to Co(IV).[51, 52] Furthermore, the pre-edge feature corresponding to the nominal Co(1s → 3d) transition, which blue-shifts to 7710.9(1) eV, significantly increases in intensity, demonstrating that the complex retains a non-centrosymmetric coordination environment about cobalt.[53] This increase in intensity is consistent with the formation of a short Co-ligand bond upon the oxidation of **1** to **2**,[54, 55] or a change in coordination geometry about the Co-center upon the oxidation of **1** to **2** (i.e., Co is contained in a quasi-tetrahedral coordination environment).[53] Lastly, a second weak pre-edge feature appears at 7716.3(2) eV; the origin of this feature will be discussed in detail below (Section 2.7).

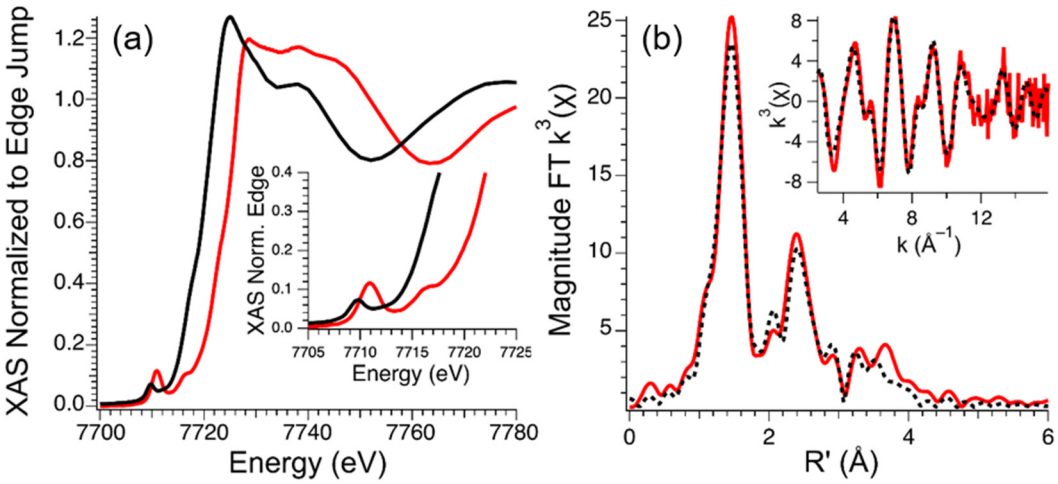

Figure 3. (a) XANES region of the cobalt K-edge X-ray absorption spectrum of **1** (black) and **2** (red). Inset displays the pre-edge feature corresponding to the nominal Co(1s → 3d) transition. (b) Magnitude Fourier transformed k^3-weighted EXAFS region of the cobalt K-edge X-ray absorption spectrum depicting the experimental data (solid red spectrum) and best fit to the data (dashed black spectrum). Inset: k^3-weighted EXAFS region of the cobalt K-edge X-ray absorption spectrum depicting the experimental data (solid red spectrum) and best fit to the data (dashed black spectrum). Best fit to the EXAFS data of **2**: E_o = 7722.3 eV; Shell #1: Co-O n = 1; r = 1.706(4) Å; σ^2 = 0.0013(4) Å^2; Shell #2: Co-N n = 3; r = 1.880(2) Å; σ^2 = 0.0028(2) Å^2; Shell #3: Co-N n = 1; r = 2.244(8) Å; σ^2 = 0.0025(6) Å^2; Shell #4: Co-C n = 3; r = 2.806(5) Å; σ^2 = 0.0054(5) Å^2; Shell #5: Co-C n = 5; r = 3.158(5) Å; σ^2 = 0.0044(5) Å^2; Shell #6: Co-C n =8; r = 4.178(8) Å; σ^2 = 0.0061(8) Å^2; ε^2 = 1.06.

The EXAFS region of the cobalt K-edge X-ray absorption spectrum of **2** is best modeled with Co contained in a four-coordinate ligand environment with three Co-N scatterers at 1.88 Å and a short Co-O scatterer at 1.71 Å (Table S3). A longer Co-N vector could further be located at 2.24 Å, which is well separated from the shorter Co-N ligand donors, and the longer Co-C scatterers comprising the ligand framework. In addition to this four-coordinate model, a statistically significant five-coordinate model to the EXAFS data can also be located (see supporting information). Taken together, the Co K-edge X-ray absorption data therefore suggests that **2** is a Co(IV)-oxo complex in either a four-coordinate quasi-tetrahedral coordination environment or a five-coordinate square pyramidal coordination environment; however, detailed spectroscopic and computational studies support a four-coordinate quasi-tetrahedral coordination environment for the Co(IV) ion of **2** (vide infra).

2.3. Resonance Raman Spectroscopy

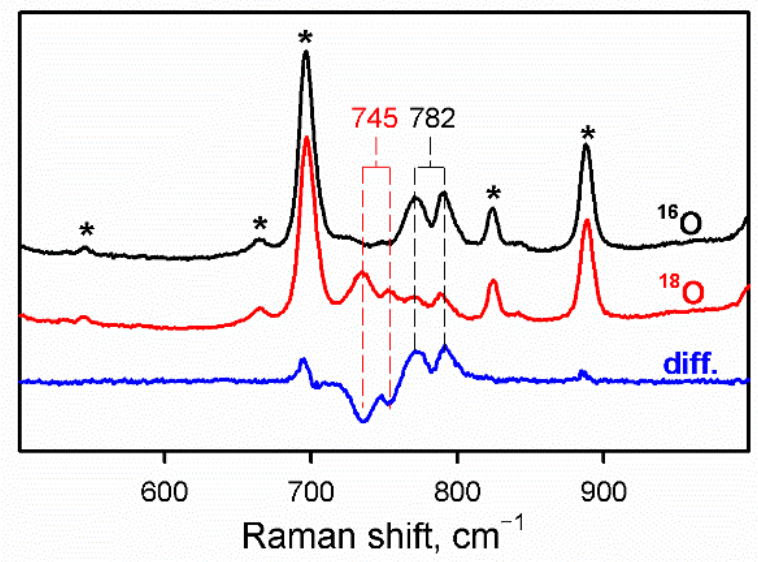

Figure 4. rRaman spectra of **2**-^{16}O (6.0 mM, black line) and **2**-^{18}O (6.0 mM, red line) obtained upon 442 nm laser excitation in acetone-d_6/TFE (*v/v* = 4:1) at –40 °C. The blue line corresponds to the difference spectrum of **2**-^{16}O and **2**-^{18}O. The peaks marked with an asterisk (*) originate from solvents.

The presence of an oxo ligand in **2** was further confirmed by rRaman spectroscopy. The rRaman spectrum of **2** obtained upon 442 nm laser excitation in acetone-d_6/TFE (v/v = 4:1) at –40 °C shows two isotopically sensitive features centered at 782 cm^{-1}, which shift to lower energy upon ^{18}O-incorporation (Figure 4). In the latter case, two new bands are observed, but with much altered relative intensities (centered at 745 cm^{-1}). We attribute the splitting of the Co-O stretch to mixing with other vibrations in this energy region. An alternative explanation is that there are two structurally similar Co-oxo species present in solution, giving two rRaman bands in the ^{16}O- and ^{18}O-labeled complexes. However, if the two signals observed in the rRaman data around 782 cm^{-1} would originate from two slightly different forms of the complex, then upon ^{18}O labeling, these two bands would simply move to lower energy without a change in their relative intensities. This is not observed experimentally. Based on our data, we therefore favor the model where mode mixing causes a splitting of the Co-O stretch. The observed isotopic shift of $\Delta\nu \approx 37$ cm^{-1} upon ^{18}O-incorporation is in good agreement with the calculated value of $\Delta\nu = 36$ cm^{-1} expected for a diatomic Co–O oscillator (Hooke's Law). It should be noted that the energy of the Co-O stretching vibration in **2**, centered at 782 cm^{-1}, is 12 cm^{-1} higher than the Co-O stretch of the related complex $[Co^{IV}(O)(13\text{-TMC})]^{2+}$ (772 cm^{-1}) bearing a similar supporting ligand.[50] However, this Co-O stretching frequency is still lower than that of cobalt oxide, Co_3O_4 (ν(Co-O) = 840 cm^{-1}),[24] and the corresponding Fe-O stretch in mononuclear nonheme Fe^{IV}-O complexes (ν(Fe-O) = 820 – 850 cm^{-1}).[56, 57] Therefore, we conclude that **2** contains a Co-oxo moiety, with a somewhat weak Co-O bond and that this species does not correspond to a Co-hydroxide complex.

Figure S3 further shows a comparison of the rRaman spectrum of **2** with that of the solvent only, to identify other rRaman signals originating from the Co-oxo unit and the NH group putatively formed by ligand protonation (vide infra). Unfortunately, no further signals could be identified in these experiments (see Figures S3 – S5).

2.4. EPR Spectroscopy

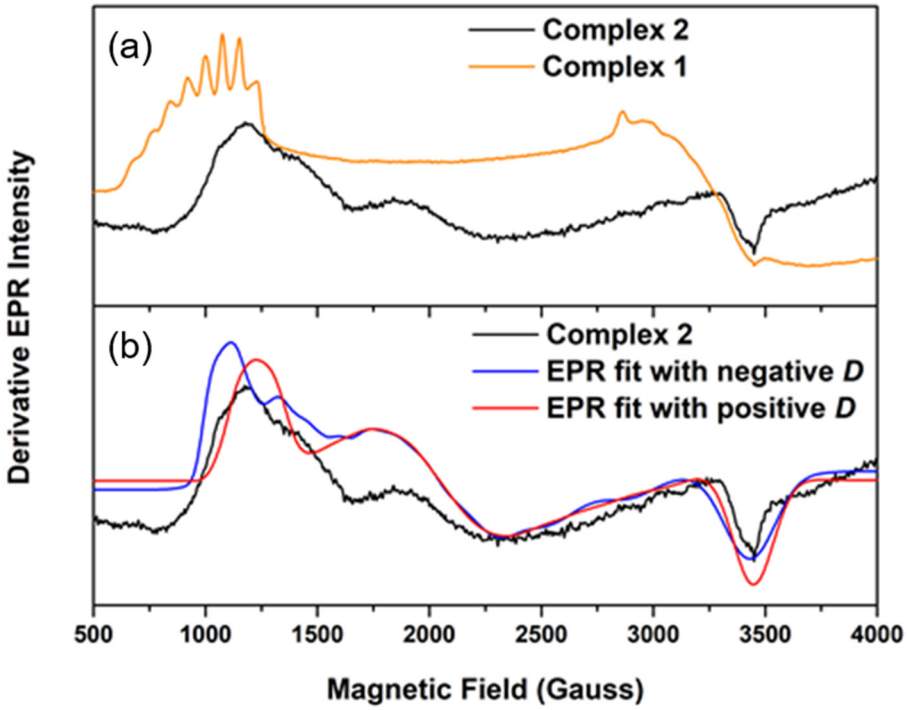

Figure 5. (a) X-band EPR spectra of the Co(II) precursor **1** (orange line) and the high-valent complex **2** (black line) recorded in acetone/TFE (*v/v* = 4/1) at 5 K. The X-band EPR spectrum of **2** shows signals at g_{eff} = 5.9, 3.4, and 2.00. (b) Fits of the EPR spectrum of complex **2** using the following parameters: g_x = 2.15, g_y = 2.18, g_z = 2.14, D = –6 cm^{-1} and E/D = 0.16 (blue line) and g_x = 2.20, g_y = 2.25, g_z = 2.15, D = 5 cm^{-1} and E/D = 0.17 (red line). EPR fits were performed with the program Spin Count by Hendrich and co-workers.[58]

EPR spectroscopy was used to further investigate the spin state of the complex. Figure 5a shows the EPR data of the Co(II) precursor **1**, which has an S = 3/2 ground state with clearly distinguishable Co hyperfine coupling for the signal around g_{eff} = 7.2. Upon reaction with PhIO, complex **2** forms, which has clearly distinct EPR features from **1**, with g_{eff} = 5.9, 3.4 and 2.00. We initially attempted to fit these data with an S = 5/2 ground state as shown in Figure S6; however, this leads to a fit of insufficient quality, especially with respect to the broad signal between 2000 and 3000 G (g ~3.4) that cannot be reproduced with the S = 5/2 spin state. On the other hand, the spectrum can be fitted well if we assume an S = 3/2 total spin, as shown in Figure 5b. We can

readily achieve a good fit of the data with g_x = 2.15, g_y = 2.18, g_z = 2.14, D = –6 cm^{-1}, and E/D = 0.16. If D is assumed to be positive, the data can be fit with slightly larger g values (g_x = 2.20, g_y = 2.25, g_z = 2.15) and a similar E/D = 0.17. The high degree of rhombicity obtained from the fit is surprising and does not agree with the initially assumed tetragonal structure of the complex (see Figure 1e). A tetragonal N4Co=O unit would show an axial EPR spectrum with E/D ~0, in agreement with the DFT and CASSCF/NEVPT2 results for such a structure (see below Section 2.5). Together with the EXAFS results, this clearly indicates that the structure of the complex **2** is no longer four-fold symmetric, but instead, this finding further supports a distorted tetrahedral structure for **2**.

With this result in mind, the question then arises what the origin for this structural distortion could be. In this regard, it should be noted that the complex **2** only forms in the presence of a proton source, which is not unusual, and has been noted for [Co(13-TMC)(O)]$^{2+}$ as well.[50] Thus, we started to suspect that the complex might be protonated, and based on the Co-O stretch that indicates the presence of a Co-oxo (and not hydroxo) unit, the most logical assumption is a protonation of the 12-TBC co-ligand. These ideas were further explored using DFT calculations.

2.5. Density Functional Theory (DFT) Calculations

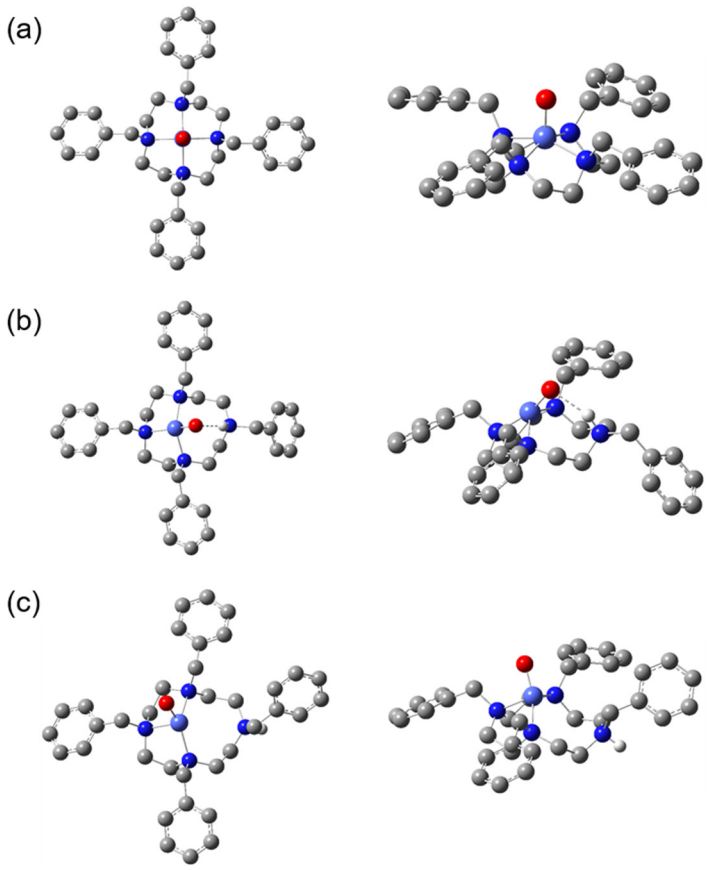

Figure 6. DFT-optimized structures with B3LYP/TZVP of tetragonal $[Co(12\text{-}TBC)(O)]^{2+}$ (a) and of the two isomers of $[Co\{H(12\text{-}TBC)\}(O)]^{3+}$ where one of the tertiary amine groups of the ligand is protonated (all S = 3/2) (b and c). In (b), the proton is hydrogen bonding with the oxo unit, whereas in (c) the proton is facing away from the Co-oxo group. In both (b) and (c), the protonation breaks the tetragonal symmetry of the Co(12-TBC) unit. The structure in (b) shows a Co=O---HN hydrogen bond and is energetically favored by >10 kcal/mol, compared to the structure in (c), which lacks the hydrogen bond.

In order to analyze the structural distortions arising from ligand protonation in complex **2** and the implications for electronic structure, we turned to DFT calculations. Since we know from EXAFS and rRaman that the complex contains a Co-oxo unit, and not Co-hydroxo, we then investigated the two possible protonated structural isomers shown in Figures 6b and 6c that could potentially form under our reaction conditions. Each structure was fully optimized using B3LYP/TZVP and PBE0/TZVP with S = 3/2 as determined from EPR spectroscopy. While this works straightforwardly for the unprotonated tetragonal complex (Figure 6a and Table 1), optimization

of the protonated structures (with and without the Co=O---HN hydrogen bond) leads to the oxidation of the benzyl groups and creation of a $H(12\text{-}TBC)^{2+\bullet}$ ligand radical with a bound Co(III)-oxo group (see Table S4 for the calculated spin distributions). This electronic structure, however, is not in agreement with the XAS data, and therefore represents an artifact from the DFT calculations. TD-DFT calculations further predict that formation of a benzyl radical would lead to the appearance of intense $\pi \rightarrow \pi^*$ transitions in the NIR absorption spectra, which is not observed either experimentally. Therefore, the valence tautomer that shows benzyl group oxidation and reduction of the Co center can be ruled out for **2**. Interestingly, inclusion of an acetone solvent field in the DFT calculations is able to remediate this problem (with the exception of the PBE0 calculation on the protonated complex that lacks the hydrogen bond), leading to minimal spin densities on the 12-TBC co-ligand. Table 1 provides a comparison of the DFT-calculated structural and spectroscopic properties with our experimental data. CASSCF/NEVPT2 calculations were further used to provide a higher-level view of the EPR parameters. These results agree well with the DFT calculations, as shown in Table 1 (also see Figure S7). The tetragonal Co-oxo complex gives good agreement with the structural data (exp. Co-O bond length: 1.71 Å versus calculated: 1.69 – 1.70 Å) but does not reproduce the experimental EPR parameters and the tetrahedrally distorted structure (from EXAFS). As dictated by symmetry, the tetragonal complex should give a very axial EPR spectrum with a predicted D = –3 to –5 cm^{-1} and E/D = 0, which sharply deviates from our EPR results.

Upon ligand protonation, but in the absence of a Co=O---HN hydrogen bond, the structure about the Co center becomes distorted trigonal-pyramidal (Figure 6c), and hence, rhombic. Our DFT calculations are very consistent and estimate the E/D for such a structure to be ~0.20, which is close to experiment. Interestingly, the reduced coordination number compared to the tetragonal structure leads to a distinct decrease in the predicted Co-O distance (calculated: ~1.61 Å with B3LYP/TZVP; note that the PBE0/TZVP calculation still gives the wrong ground state, as

mentioned above), which deviates significantly from experiment. The protonated amine group of the ligand is flipped around and points away from the Co center, as shown in Figure 6c. The resulting Co-N distance is 3.79 Å.

Finally, the ligand protonated structure in Figure 6b features a Co=O---HN hydrogen bond, which further distorts the geometry of the complex. The resulting geometry about the Co center is best described as a seesaw (i.e., a trigonal bipyramid where one of the corners in the trigonal plane is empty). DFT calculations predict this structure, $[Co(12\text{-}TBC)(O\text{---}HN)]^{3+}$, to be >10 kcal/mol lower in energy compared to the ligand protonated structure that lacks the hydrogen bond (see Figures 6b and 6c). Although the B3LYP- and PBE0-calculated structures overlay almost perfectly (see Figure S8), they show some differences in the calculated EPR properties (see Table 1). In particular, B3LYP predicts E/D = 0.15, which is in excellent agreement with experiment, whereas PBE0 yields a calculated E/D ~0.3, which overestimates the degree of rhombicity. The CASSCF/NEVPT2 calculations give E/D = 0.14 for this structure, which matches the B3LYP-calculated and experimental E/D. The calculated g values are in good agreement with the experimental data, considering that they are often underestimated by DFT. It is also notable that the DFT and CASSCF/NEVPT2 calculations, across the board, predict the D value to be negative. From the EPR simulation, we predict that $|D|$ = 4 – 7 cm^{-1}, which is in excellent agreement with the DFT and CASSCF/NEVPT2 results, but we lack the ability to unequivocally predict the sign of D (see Figure 5b) from the EPR data. However, based on the highly consistent DFT results, we conclude that D is negative. In terms of the Co-O distance, we note that the hydrogen bond leads to an elongation of the Co-O bond length (~1.65 Å), compared to the structure that lacks the hydrogen bond (1.61 Å). The EXAFS fit estimates the Co-O distance at 1.71 Å, which agrees well with the DFT predictions. The EXAFS data further support the overall distorted tetrahedral structure of **2**. The average Co-N distance of 1.88 Å compares reasonably well with the computed value of 1.99 Å. Finally, due to the hydrogen bond, the Co-N distance of

the protonated amine is shorter compared to the structure without the hydrogen bond, predicted at ~3.32 Å.

While the DFT calculations are highly successful in reproducing the structural and EPR-spectroscopic properties of **2**, some deviations are observed for the Co-O stretch. Of the three different structures evaluated for **2**, the ligand protonated complex without the hydrogen bond shows the most significant deviation from the experimental value (782 cm^{-1}), and greatly overestimates the Co-O stretch. The other two structures lead to better agreement, and generally underestimate the vibrational frequency of this mode (see Table 1). However, considering the spread in DFT-predicted frequencies, no further conclusions were drawn from these results.

In summary, we propose that the structural distortions of **2** identified by spectroscopy originate from protonation of the complex. The unique Co=O---HN hydrogen bonding interaction that is proposed to form in **2** stabilizes the Co-oxo complex and breaks the tetragonal symmetry, which is in agreement with our experimental data. Based on these results, we conclude that the ligand-protonated structure with the NH hydrogen bond pointing towards the oxo ligand (Figure 6b) is the best structural model for **2**, as this model reproduces all available spectroscopic data. We then used this model for the further analysis of the optical properties of **2**. Because of this, "$[Co(12\text{-}TBC)(O)]^{2+}$" should actually be designated as $[Co\{H(12\text{-}TBC)\}(O)]^{3+}$ or $[Co(12\text{-}TBC)(O\text{---}HN)]^{3+}$.

Table 1. Comparison of Experimental and Calculated Structural and Spectroscopic Properties of **2**

Calculation type	Co-O (cm^{-1})	d(Co-O) (Å)	Spin density			D (cm^{-1})	E/D	g-tensor	Rel. Energy (kcal/mol)
			Co	O	ligand				
N-protonated <u>with</u> hydrogen bond to Oxo complex									
Exp. Data	782	1.71	N/A	N/A	N/A	–6	0.16	[2.15, 2.18, 2.14]	-
						5	0.17	[2.20, 2.25, 2.15]	-
B3LYP/TZVP [a]	747	1.65	2.00	0.94	0.06	–3	0.15	[2.04, 2.06, 2.11]	0
PBE0/TZVP [a]	700	1.64	2.02	0.95	0.03	–4	0.30	[2.04, 2.06, 2.11]	0
CASSCF/NEVPT2	-	-	1.97	0.97	0.06	–5	0.14	[2.05, 2.08, 2.13]	-
N-protonated <u>without</u> hydrogen bond to Oxo complex									
B3LYP/TZVP [a]	873, 885 [b]	1.61	2.08	0.88	0.04	–3	0.22	[2.04, 2.04, 2.08]	+12
PBE0/TZVP [a]	797	1.65	2.69	1.05	–0.74 [c]	–8	0.18	[2.04, 2.06, 2.10]	+24
Non-protonated Oxo complex									
B3LYP/TZVP	765	1.70	1.74	1.35	–0.09	–3	0.00	[2.02, 2.05, 2.05]	-
PBE0/TZVP	764	1.69	1.74	1.38	–0.12	–5	0.00	[2.02, 2.05, 2.05]	-
CASSCF/NEVPT2	-	-	1.56	1.52	–0.08	–5	0.00	[2.03, 2.04, 2.04]	-

[a] Calculated with an acetone solvent field. [b] Coupled to ligand C-H wagging vibrations. [c] In this calculation, the ligand $H(12\text{-}TBC)^+$ is oxidized, evident from a calculated spin density on the ligand of –0.74.

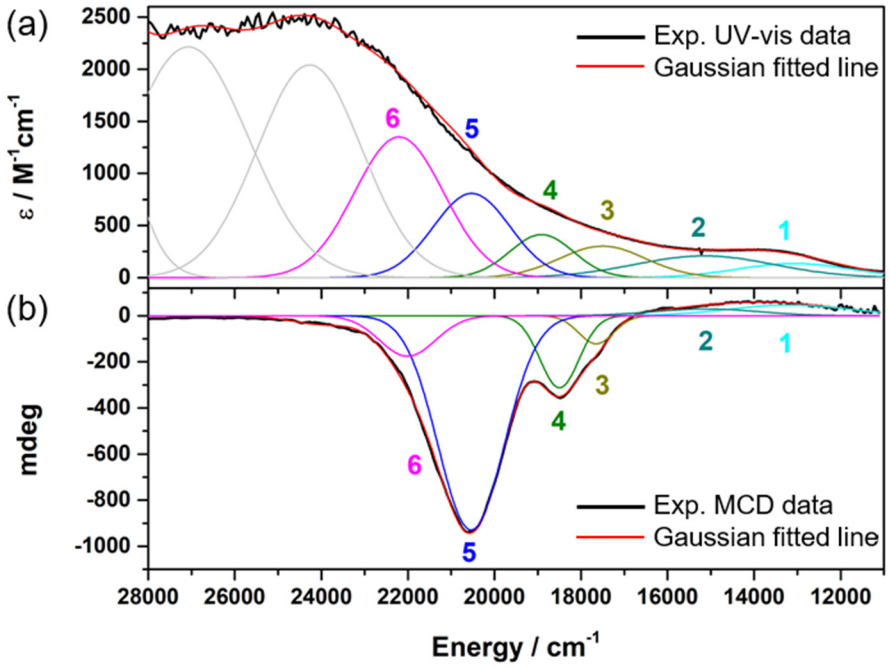

Figure 7. (a) UV–vis spectrum of complex **2** (1.0 mM) at –40 °C. (b) MCD data of complex **2** (4.0 mM) measured at 2 K and 7 T.

2.6. UV-vis and MCD Spectroscopy

The UV-vis spectrum of complex **2**, shown in Figure 7, exhibits a weak signal at 720 nm (band no. 1 in Figure 7) that grows upon formation of the oxo complex (see Figure 2) and broad features in the higher energy region. To gain further insight into the nature of these electronic transitions, we then performed low-temperature MCD experiments on complex **2**, using variable temperatures between 2 – 50 K and magnetic field strengths from 0 to 7 T. Figure 7 shows a direct comparison between the UV-vis and the MCD spectra of the complex, along with a correlated fit of these data. Besides the weak feature at 720 nm, the MCD spectrum exhibit two major signals at 485 and 541 nm (band nos. 5 and 4, respectively, in Figure 7). All of these signals are temperature-dependent (see Figure S9) and therefore correspond to MCD **C**-term signals. In comparison, the MCD spectrum of the Co(II) precursor **1** is featureless, and the decomposition product of **2** exhibits a completely different MCD spectrum with very broad features that are really low in intensity (see

Figures S10 and S11). Based on these findings, we are confident that the data shown in Figure 7 correspond to the authentic optical spectra of the Co-oxo complex **2**.

Table 2. Summary of Gaussian Deconvolution of the Optical Spectra of Complex **2**, in Direct Comparison to the TD-DFT Calculations (B3LYP/TZVP)

No.	MCD		UV-vis		Assignment	Polarization (%)[a]
	Energy (cm^{-1})	mdeg	Energy (cm^{-1})	ε ($M^{-1}\,cm^{-1}$)		
1	13184	46	13068	135		n. d.
2	15101	29	15151	208		n. d.
3	17650	–122	17503	302		n. d.
4	18497	–312	18914	413	oxo-to-Co(IV) CT	15 (x), 8 (y), 77 (z)
5	20540	–929	20526	808	oxo-to-Co(IV) CT	22 (x), 8 (y), 70 (z)
6	22009	–176	22206	1350		n. d.

[a] n. d. = not determined

The optical spectra of the Co-oxo species can be deconvoluted into five individual electronic transitions as listed in Table 2. To derive polarizations for the main transitions observed in the MCD spectra, the variable-temperature variable-field (VTVH) data for bands 4 and 5 are analyzed in Figure 8. The VTVH data for band 4 show distinct nesting, which rules out an S = 1/2 ground state for the complex, in agreement with the EPR data. The saturation curves obtained from the VTVH measurements were fitted using the ground state magnetic properties obtained from the EPR fit, as listed in Table 1 (negative D). Using these parameters for D, E/D and the g values and a spin of S = 3/2, the fits shown in Figure 8 were obtained. The results show that both bands have mixed polarizations with x, y, and z contributions, which is not surprising, considering the strongly distorted structure of **2**. The dominant contribution, however, is z polarization. The numbers in square brackets in Figure 8 give a range for the polarizations, when g_x and g_y are varied between 2.15 – 2.25 and D is varied between –5 to –7 cm^{-1}. These ranges show that the polarizations observed for bands 4 and 5 in Table 2 (also see Figure 7) are stable within this parameter space.

In order to map these polarizations back onto the molecular coordinate system, we used the orientation of the principal axes of the ZFS tensor obtained from the B3LYP/TZVP calculations. As shown in Figure S12, the principal *z*-axis of the tensor is closely aligned with the Co-O bond, whereas the *x* and *y* directions do not align with any Co-ligand bond vector. The *x* component points downward and dissects one of the N-Co-N planes (see Figure S12). Based on these results, both bands 4 and 5 are assigned to oxo-to-Co(IV) charge transfer (CT) transition, apparent from their large degree of *z* polarization. This is further supported by the strong MCD and medium strong UV-vis absorption intensity of band 5, which is typically observed for CT transitions.[59, 60] Finally, this is supported by the observed resonance enhancement of the Co-O stretch upon excitation at 442 nm (22625 cm^{-1}), which is in the foot of band 5, providing further evidence for the presence of a oxo-to-Co(IV) CT transition in this spectral region.

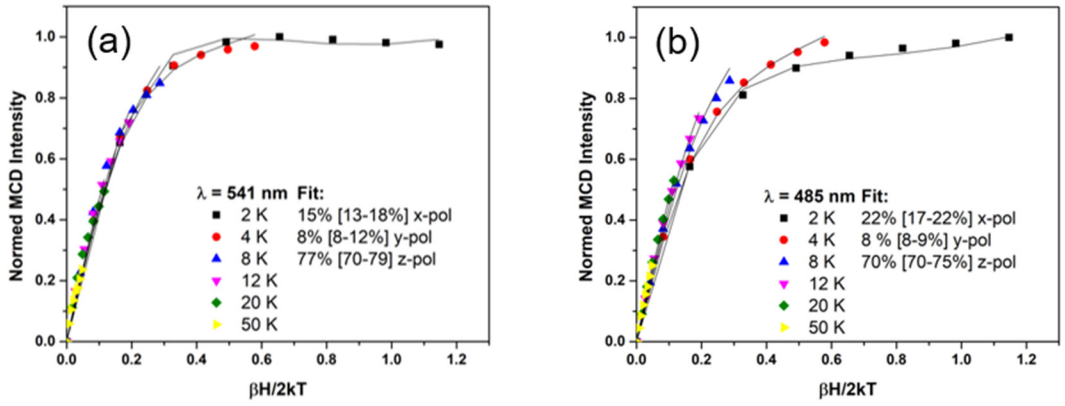

Figure 8. Saturation magnetization curves of the bands 4 and 5 (in Figure 7) at 541 nm (a) and 485 nm (b) (data points), and fits of these data (black lines) using the magnetic parameters determined from the EPR fit: $D = -6\ cm^{-1}$, $E/D = 0.16$, $g_x = 2.15$, $g_y = 2.18$, $g_z = 2.14$.

In summary, the analysis of the VTVH MCD data further supports an $S = 3/2$ ground state for **2**. The experimentally derived polarizations indicate that the major electronic transitions around 20,000 cm^{-1} arise from CT transitions with dominant oxo-to-Co(IV) CT character. The successful fit of the VTVH MCD saturation curves further provides strong support for the accuracy of the ZFS

parameters for **2**, and the negative *D* value, as derived from the EPR fit (see above). Unfortunately, band 1 at 720 nm could not be further analyzed, due to its weak MCD intensity.

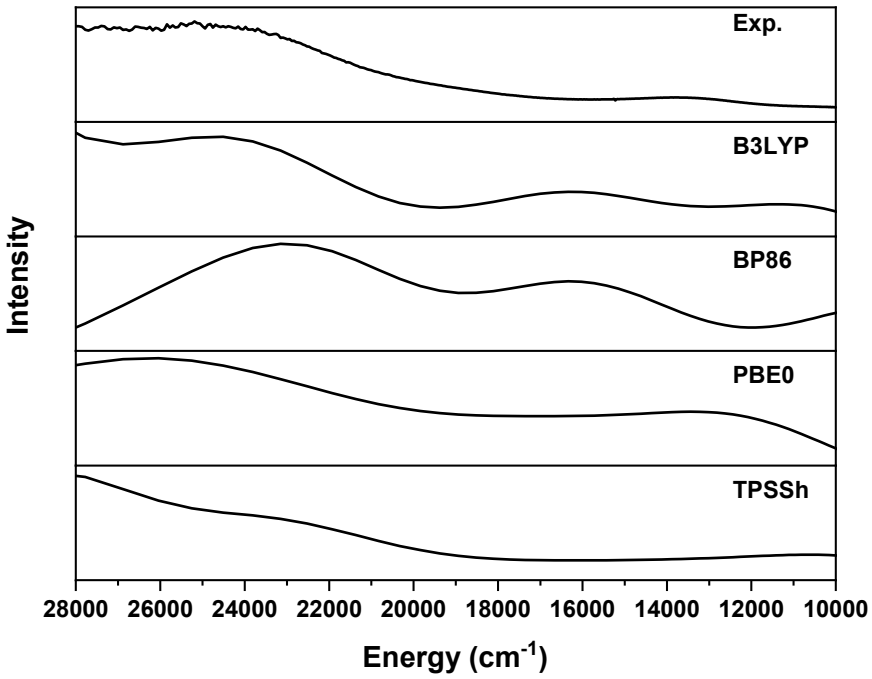

Figure 9. Comparison of the experimental UV-Vis spectrum of 1 mM **2** in acetone to those generated by TD-DFT calculations (on the B3LYP/TZVP optimized structure of $[Co\{H(12\text{-}TBC)\}(O)]^{3+}$ with the Co=O---HN hydrogen bond; see Figure 6b). Each of the spectra were calculated with TZVP as the basis set, using an acetone solvent field and the indicated functional.

To further understand the nature of the observed electronic transitions, we performed TD-DFT calculations on the ligand-protonated structure of **2** with the Co=O---HN hydrogen bond. Figure 9 shows that B3LYP and PBE0 give the best agreement with the experimental absorption spectrum of **2**. In the lower energy region where bands 1 and 2 are observed, TD-DFT predicts mainly CT transitions from the co-ligand to the Co center and d-d transitions (see Table S5). Bands 4 and 5 could be assigned to oxo-to-Co(IV) CT transitions, based on the analysis of the MCD VTVH data, as described above. In agreement with this, TD-DFT predicts the oxo-to-Co(IV) π-CT transitions roughly in the 15000 - 20000 cm^{-1} range, although these transitions are distributed over quite a

number of electronic transitions in the TD-DFT results (see Table S5). Other significant transitions in this energy region predicted by TD-DFT correspond to transitions from the π-bonding Co(d)/O(p) MOs into Co(d) orbitals, which would also be z-polarized. Therefore, the TD-DFT calculations further support the spectral assignments obtained here.

2.7. Electronic Structure

The pre-edge region of the Co K-edge X-ray absorption spectrum of **2** was modeled using TD-DFT methods (PBE0/def2-tzvp(-f)/ZORA). In addition to the computational models containing a protonated ligand amine nitrogen atom hydrogen bonded to the Co(IV)-O moiety ([Co(12-TBC)(O---HN)]$^{3+}$), we also considered two five-coordinate formal Co(IV) computational models. One contained a protonated oxo ligand ([Co(12-TBC)(OH)]$^{3+}$) and the other contained an unprotonated oxo ligand ([Co(12-TBC)(O)]$^{2+}$; Figure 10). The resulting TD-DFT spectrum of [Co(12-TBC)(OH)]$^{3+}$ is inconsistent with the available data – it produced a pre-edge feature that was weak relative to the experimental data and did not reproduce the weak transition ~5 eV higher than the pre-edge observed in the experimental data. Owing to increased mixing of Co(4p) character into the low-energy acceptor states resulting from the short Co-O bond, the pre-edge feature is better reproduced by TD-DFT with unprotonated ([Co(12-TBC)(O)]$^{2+}$. However, similar to [Co(12-TBC)(OH)]$^{3+}$, this computational model does not reproduce the weak transition ~5 eV higher in energy than the pre-edge transition observed in the experimental data.

In contrast to these two formal Co(IV)-oxo species, the four-coordinate model [Co(12-TBC)(O---HN)]$^{3+}$ reproduces both the pre-edge transition and the higher energy feature observed in the XANES. Owing to both the low-symmetry about Co and the short Co-O bond, the pre-edge transition gains intensity through mixing of Co(4p) character into the Co(3d) dominated acceptor states. The feature that is approximately 5 eV higher in energy results from a transition into a ligand π* dominated final state (a Co(1s) → L(π*) transition). As demonstrated by single crystal

XAS studies of $[Cu(bpy)_2]^{2+/+}$ complexes by Lancaster and co-workers,[61] these transitions are best thought of as Co(1s → 4p) transitions, not XAS-MLCT transitions; although the acceptor state is dominated by oxygen, nitrogen and phenyl carbon 2p character, the minor degree of Co(4p) character (~2% Co(4p)) in the L(π*) acceptor state allows the transition to gain intensity.

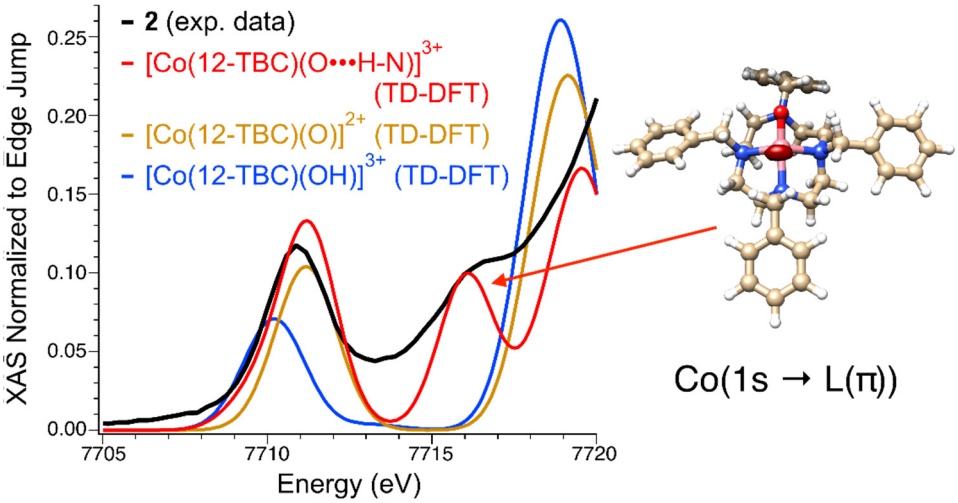

Figure 10. Experimental Co K-edge X-ray absorption spectrum of **2** (black) and TD-DFT calculated Co K-edge X-ray absorption spectra (PBE0/def2-tzvp(-f)/ZORA) of $[Co(12\text{-}TBC)(O\text{---}HN)]^{3+}$ (red), $[Co(12\text{-}TBC)(OH)]^{3+}$ (blue) and $[Co(12\text{-}TBC)(O)]^{2+}$ (gold). The isosurface plot (0.005 au cut-off) depicts the transition density plot of the dominant acceptor state comprising the feature found ~5 eV higher in energy than the pre-edge transition for $[Co(12\text{-}TBC)(O\text{---}HN)]^{3+}$.

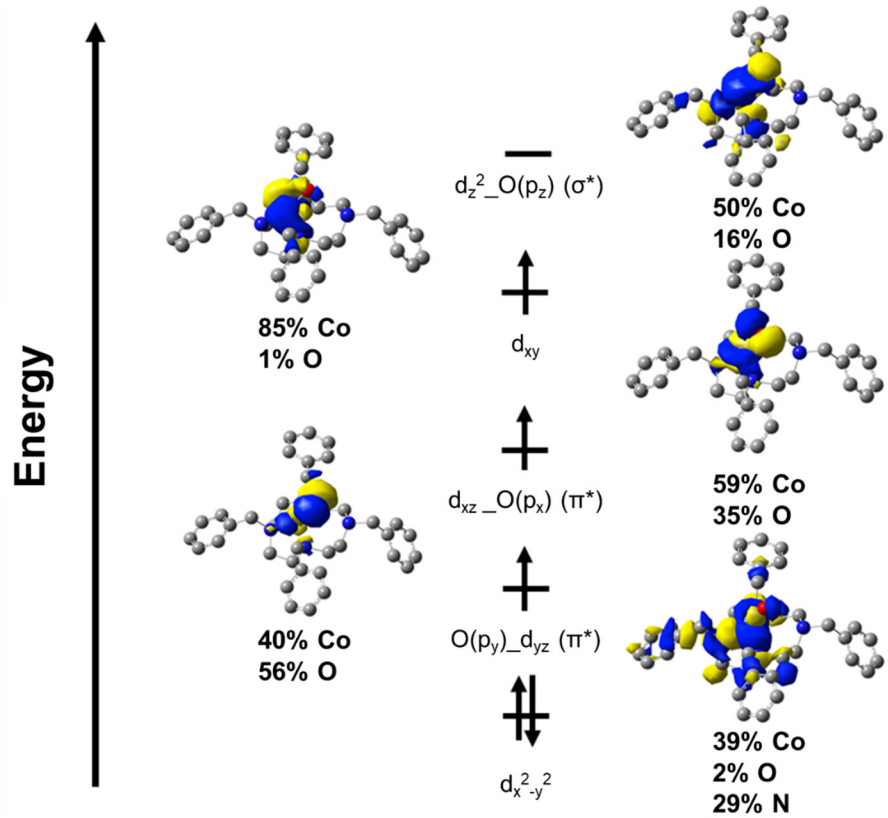

Figure 11. MO diagram of the ligand-protonated Co(IV)-oxo complex $[Co\{H(12\text{-}TBC)\}(O)]^{3+}$ with the NH---O=Co hydrogen bond, generated using unrestricted natural orbitals (UNOs; obtained with PBE0/TZVP). In the labeling scheme applied here, for example "O(p_y)_d_{yz}", the orbital "O(p_y)" listed first makes the larger contribution than "d_{yz}" to the resulting molecular orbital "O(p_y)_d_{yz}".

To further elucidate the electronic structure of the ligand-protonated and Co=O---HN hydrogen-bonded form of **2**, the PBE0/TZVP-calculated wave function was analyzed using unrestricted natural orbitals. Complex **2** has an intermediate spin state (*S* = 3/2) with five valence electrons, with one of the d-orbitals being doubly occupied. The resulting MO diagram is shown in Figure 11 (also see Tables S6 and S7). The lowest unoccupied molecular orbital (LUMO) corresponds to the antibonding combination of the d_{z2} orbital of Co and the O(p_z) orbital (d_{z2}_O(p_z), 50% Co and 16% O), which is found at high energy due to the strong Co-O σ-bond. In the applied coordinate system used here with the x direction along the Co=O---HN hydrogen bond (see Scheme 2), the highest singly occupied molecular orbital (SOMO) corresponds to the

d_{xy} orbital (85% Co), which interacts with some of the nitrogen atoms of the $H(12\text{-}TBC)^{+}$ co-ligand. This is followed by the SOMO-1 and SOMO-2, which correspond to the two π-antibonding interactions between the d_{xz} and d_{yz} orbitals of Co and the $O(p_x)$ and $O(p_y)$ lone pairs. The SOMO-1, d_{xz}_$O(p_x)$, has 59% Co and 35% $O(p_x)$ character, and corresponds to a typical metal-oxo π* orbital in which the major contribution originates from the metal center. On the other hand, the SOMO-2, $O(p_y)$_d_{yz}, shows an inverted interaction, where the resulting π* orbital now has 40% Co and 56% $O(p_y)$ contributions, and hence, dominant oxo character. As we move from the left to the right in the periodic table, the effective nuclear charge of the transition metal ions increases, thus lowering their d orbitals in energy. If the d orbitals drop in energy below the O(p) donor orbitals, then the doubly-occupied bonding MOs will now have dominant metal character, whereas the partly occupied, antibonding MOs have dominant ligand character. In a case where the antibonding orbitals are singly occupied, this effectively corresponds to an oxidation of the ligand, creating distinct radical character on the ligand (see Scheme 3). Inverted metal-ligand bonding schemes have recently been elucidated in a number of high-valent mid- and late-first row transition metal species, suggesting this may be a common yet under-appreciated feature of such systems.[62-64]

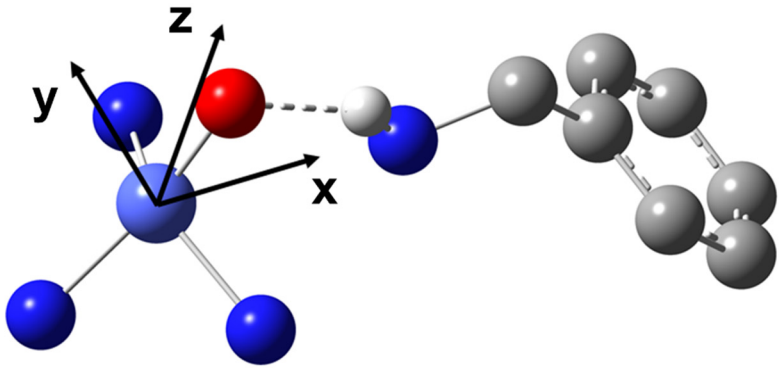

Scheme 2. Coordinate system used for the MO discussion. The structure is derived from the optimized structure of $[Co\{H(12\text{-}TBC)\}(O)]^{3+}$ using PBE0/TZVP.

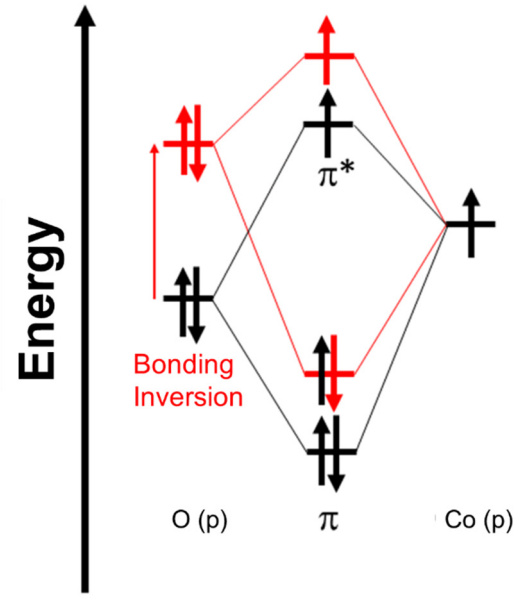

Scheme 3. Normal (black) versus inverted (red) bonding scheme for the Co-O π bond.

This interesting dichotomy between the two Co-oxo π-bonds relates back to the presence of the Co=O---HN hydrogen bond, which is located along the x-axis (in our coordinate system, see Scheme 2). Here, the hydrogen bond stabilizes the O(p_x) orbital, which shifts this orbital to lower energy and causes the normal Co-O π-interaction. In contrast, without the hydrogen bond, the Co-O π-interaction becomes inverted (see Scheme 3). This finding has general implications and shows how second coordination sphere (SCS) interactions can tune late transition metal-oxo bonds, which are on the borderline of bond inversion.[30] This is important for the reactivity of these complexes, as bond inversion increases the amount of radical character on the oxo ligand, giving it distinct oxyl character, and this is thought to increase the reactivity of the metal-oxo unit towards H-atom abstraction. In the case of $[Co\{H(12\text{-}TBC)\}(O)]^{3+}$, the DFT calculations indicate that the bond inversion is quite small, and this finding is supported by XAS results (see above) which show a large shift in the Co K edge upon formation of the Co-oxo complex, indicating that this species

is best described as a Co(IV) complex with two very covalent Co-oxo π-bonds (and not a Co(II) complex, which would imply a significantly enhanced degree of ligand oxidation).

The last valence orbital of the complex is the SOMO-3, which is doubly occupied and corresponds to the d_{x2-y2} orbital in our coordinate system. This orbital shows strong ligand contributions, with 39% Co and 29% N character. We note that the NEVPT2 calculations of **2** demonstrate that the complex, although well described using hybrid-DFT methods, possesses a moderate degree of multiconfigurational resulting from promotion of Co-O bonding electrons into Co-O antibonding orbitals (see Supporting Information). Furthermore, the NEVPT2 calculations also demonstrate that the high energy Co-N* antibonding orbital has partially occupancy as opposed to being doubly occupied. This is the likely origin of the deviation in the calculated vs experimentally derived bond lengths. The additional antibonding character of the Co-O bond would be expected to lead to an elongation of the Co-O bond length while the reduction in Co-N antibonding character will lead to a net reduction in the Co-N bond length.

2.8. Reactivity

The reactivity of the Co(IV)-oxo complex (**2**) was investigated in hydrogen atom transfer (HAT) and oxygen atom transfer (OAT) reactions. The oxidation reactions with weak C–H bonds substrates were carried out with *in situ* generated **2**. Addition of xanthene to a solution of **2** in acetone/TFE (*v/v* = 4:1) at –40 °C resulted in the disappearance of **2** with a first-order decay profile (Figure 12a). The first-order rate constants, determined by pseudo-first-order fitting of the kinetic data for the decay of **2**, increased linearly with the increase of xanthene concentration (Figure 12b), giving a second-order rate constant of 3.2×10^{-2} M^{-1} s^{-1}; this reaction is slower than the reaction of $[Co^{IV}(13\text{-TMC})(O)]^{2+}$ with xanthene since the second-order rate constant in acetone at –40 °C was 1.5×10^{-1} M^{-1} s^{-1}.[50] A kinetic isotope effect (KIE) value of 4.5(2) was obtained in the oxidation of xanthene and xanthene-d_2 by **2** (Figure 12b). We also determined the second-

order rate constant in the oxidation of 1,4-cyclohexadiene (CHD) (Figure S13). On the basis of the KIE value and the dependence of the rate constant on substrate concentration, we conclude that hydrogen atom (H-atom) abstraction from the C–H bonds of substrates by **2** is the rate-determining step (r.d.s.) in the C-H bond activation reactions. Product analysis of the xanthene oxidation by **2** revealed the formation of xanthone in 60(5)% yield. When the reaction was performed with ^{18}O-labeled **2** (**2**-^{18}O), the oxygen in xanthone was found to derive from the Co(IV)-oxo species (Figure S14). We also characterized the decay product of **2** in the xanthene oxidation using various spectroscopic methods, such as UV-vis, EPR, and CSI-MS spectroscopies (Figure S15), showing that **2** was converted to the starting $[Co^{II}(12\text{-TBC})]^{2+}$.

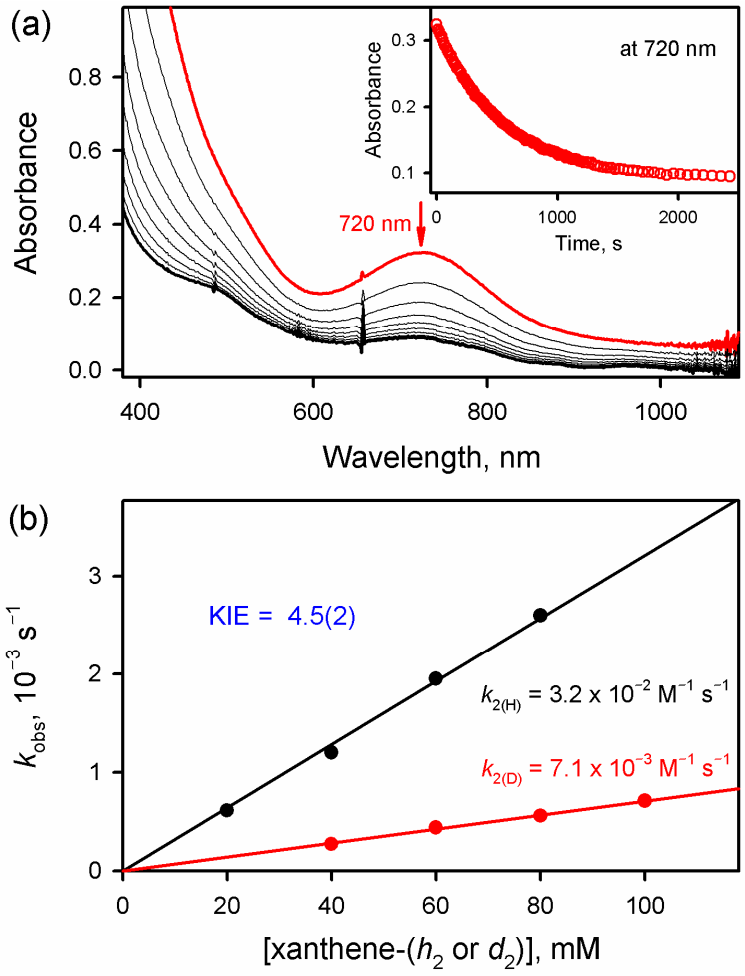

Figure 12. (a) UV-vis spectral changes observed in the oxidation of xanthene (60 mM) by **2** (0.50 mM, red line) in acetone/TFE (*v/v* = 4:1) at –40 °C. Inset shows the time trace monitored at 720 nm due to the decay of **2**. (b) Plots of k_{obs} (s^{-1}) against concentration of xanthene (black circles) and xanthene-d_2 (red circles) for the oxidation of xanthene-(h_2 or d_2) by **2** (0.50 mM) in acetone/TFE (*v/v* = 4:1) at –40 °C to determine the second-order rate constants (k_2, M^{-1} s^{-1}) and KIE value.

The reactivity of **2** was also investigated in OAT reactions (i.e., sulfoxidation of *para*-X-substituted thioanisole derivatives) in acetone/TFE (*v/v* = 4:1) at –40 °C (see Figure 13). Upon addition of thioanisole to an acetone/TFE (*v/v* = 4:1) solution of **2** at –40 °C, the absorption band at 720 nm due to **2** decreased with the first-order kinetics profile, giving the first-order rate constant (k_{obs}) of 5.8 × 10^{-3} s^{-1} (Figure 13a). The k_{obs} value was in proportion to the concentration of thioanisole to give the second-order rate constant (k_2) of 1.9(1) × 10^{-2} M^{-1} s^{-1} at –40 °C (Figure 13b). Similarly, the second-order rate constants were determined for other *para*-X-substituted thioanisole derivatives, such as *para*-MeO-thioanisole, *para*-Me-thioanisole, and *para*-F-thioanisole (Figure S16). A Hammett plot of the second-order rate constants against Hammett parameter σ_p^+ of *para*-X-substituents afforded a ρ value of –4.3 (Figure S17a and Table S8). Such a negative ρ value illustrates the electrophilic character of **2** in OAT reactions, as frequently observed in the sulfoxidation of thioanisoles by high-valent metal-oxo and metal-oxidant adduct species in heme and nonheme systems.[65-70] In addition, we observed a good linear correlation when the rates were plotted against oxidation potentials (E_{ox}) of thioanisoles (Figure S17b and Table S8). The negative slope of –15 of this correlation indicates that the oxidation of sulfides by **2** proceeds via an electron-transfer mechanism.[71]

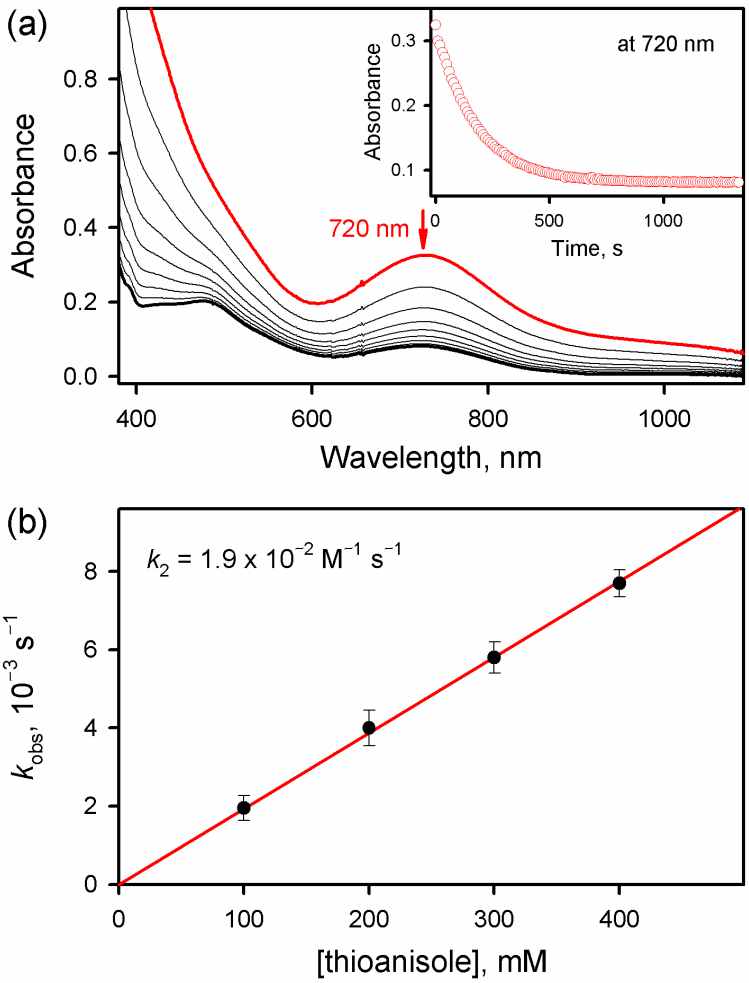

Figure 13. (a) UV-vis spectral changes observed in the oxidation of thioanisole (300 mM) by **2** (0.50 mM, red line) in acetone/TFE (*v/v* = 4:1) at –40 °C. The inset shows the time trace monitored at 720 nm due to the decay of **2**. (b) Plot of k_{obs} against concentration of thioanisole for the sulfoxidation of thioanisole by **2** (0.50 mM) in acetone/TFE (*v/v* = 4:1) at –40 °C to determine the second-order rate constant (k_2, M^{-1} s^{-1}).

Product analysis of the reaction solution obtained in the oxidation of thioanisole by **2** revealed that methyl phenyl sulfoxide was yielded as the sole product (Figure S18). In addition, based on the ^{18}O-labeling experiment performed with **2**-^{18}O, the oxygen atom in the oxide product (84(3)% ^{18}O) was found to derive from the Co–oxo group (Figure S18c). The decay product of **2** in the sulfoxidation of thioanisole was also analyzed using various spectroscopic methods, such as UV-

vis, EPR and ESI-MS spectroscopies (Figure S19), showing the conversion of **2** to the starting cobalt(II) complex.

3. Discussion

In recent years, a great interest in the late transition metal-oxo complexes developed due to their interesting properties and the expectation that these complexes could be highly active catalysts for the functionalization of C-H bond and other oxidative transformations.[30, 72] In particular, Co(IV)-oxo complexes have been the target of a number of recent studies. However, at the same time, these complexes are unstable, can often only be observed at low temperatures, and are difficult to characterize. Also, the preparation of these intermediates often requires the presence of certain additives (e.g., Brønsted and/or Lewis acids), but the roles that these additives play for the geometric and electronic structures of the complexes are often not clear. In 2017, Nam, Shearer, and co-workers reported the preparation of a Co(IV)-oxo complex with a 13-TMC co-ligand (see Figure 1), which was spectroscopically characterized along with its reactivity investigation.[50] This complex was described as $[Co(13\text{-}TMC)(O)]^{2+}$ (see Figure 1d), a five-coordinate square-pyramidal complex, but some questions remained, relating, for example, to the fact that this species can only be prepared in the presence of acid. In this study, we investigated an analogous complex $[Co(12\text{-}TBC)(O)]^{2+}$ (**2**), which uses a similar 12-TBC ligand and was prepared in a similar way from the corresponding Co(II) precursor. At a first glance, this seems like a simple task; based on the analogy of the 13-TMC and 12-TBC ligands, one would expect that these complexes behave similarly and have similar structures, as indicated in Figure 1.

Our detailed spectroscopic studies show that **2** indeed contains a Co-oxo group with a Co-O stretching frequency of 782 cm^{-1}, which is very similar to the Co-O stretch of $[Co(13\text{-}TMC)(O)]^{2+}$, observed at 770 cm^{-1}.[50] MS characterization supports the assignment of **2** as a Co-oxo complex

(see Figure 2), and Co K-edge XAS data show that the complex contains a Co(IV) center (see Figure 3). This clear-cut characterization of **2** becomes murky when the EPR data of this complex are considered. A tetragonal N4Co=O complex with four-fold symmetry should show an axial EPR spectrum with E/D ~0, which, however, is not what we observe. The EPR data show that **2** has an S = 3/2 ground state with significant rhombicity (E/D = 0.16; see Figure 5), indicating that the complex has a distorted geometry. This conclusion is also supported by the EXAFS data of this compound, which are best fit with a quasi-tetrahedral coordination environment for **2**. Our spectroscopic results therefore clearly show that **2** is not a simple N4Co=O type species with a tetragonal structure, but that the complex is strongly distorted. What the spectroscopic results do not tell us is why this is the case. Clearly, the complex would not adopt such a geometry if left to itself. Considering the experimental conditions under which **2** forms, we then explored what process could be responsible for this distortion. This is where we note again that **2** only forms in the presence of proton source. Consequently, we propose that the structural distortion of the complex is caused by protonation. We developed structural models of protonated versions of **2**, using DFT calculations. Since **2** contains an unprotonated oxo ligand, this further indicates protonation of one of the amine nitrogens of the 12-TBC ligand scaffold. Further analysis then showed that **2** corresponds to a Co-oxo complex with a Co=O---HN hydrogen bond (see Figure 6b) and a seesaw-shaped coordination geometry about the Co center. While this constitutes a certain degree of speculation, this structure is able to reproduce all spectroscopic features of **2** in our DFT and CASSCF/NEVPT2 calculations (see Table 1). The chemical formula of **2** should therefore be given as $[Co\{H(12\text{-}TBC)\}(O)]^{3+}$ or $[Co(12\text{-}TBC)(O\text{---}HN)]^{3+}$. We further propose that the hydrogen bond actually stabilizes the Co(IV)-oxo core, which is the reason why this intermediate cannot be generated (or is not stable) in the absence of acid.

Support for the proposed hydrogen bond comes from MS experiments. Here, the peak at m/z = 756.3, which corresponds to **2(OTf)**, shifts by one unit to m/z = 757.3 when the CSI-MS of **2** is

measured in acetone:TFE-d_3 and acetone-d_6:TFE-d_3 (see Figure S20). The latter results indicate that one H in $[Co(O)(12\text{-TBC})]^{2+}$ is substituted by one D in deuterated TFE. Although it is of interest to observe this deuterium exchange in deuterated TFE, this deuterium experiment does not strictly prove the presence of a Co=O---HN hydrogen bond in **2**, but it further supports our conclusions presented above.

Further analysis of the optical spectra (UV-vis and low-temperature MCD data) shows that **2** is indeed a paramagnetic species with S = 3/2. The UV-vis absorption spectrum shows a weak absorption band around 720 nm and then just a featureless rise in absorbance up to 400 nm. MCD spectroscopy is able to further resolve a number of optical transitions in the visible range, in particular an intense feature at 490 nm (= 20540 cm^{-1}), that is largely z polarized. Further analysis shows that this band corresponds to an oxo-to-Co(IV) charge-transfer transition, directly supporting the presence of an oxo ligand in **2**. This conclusion is further supported by the resonance Raman data, showing resonance enhancement of the Co-O stretch upon laser excitation in this spectral region. The success in fitting the VTVH MCD data also supports the accuracy of the EPR-derived ZFS parameters, in particular the conclusion that the complex shows a strong rhombic distortion and that D is negative.

Since hydrogen bonds are relatively weak, we further propose that the Co=O---HN hydrogen bond is a “soft” bond and likely dynamic, which means that there could be an ensemble of very similar structures present in solution that vary in the NH---O=Co distance and the N-H-O(Co) angle, especially if one considers that solvent molecules could further participate in the H-bonding interactions. Such species would then slightly differ in their EPR properties (whereas other techniques would be rather insensitive to such slight structural variations), which could contribute to the observed broadness of the EPR spectra.

As discussed in the Introduction, with an *S* = 3/2 ground state, the Co(IV)-oxo complex **2** has a formal bond order of 2 (see Scheme 1), which would constitute a violation of the famous "oxo wall".[29, 30] However, since **2** does not have a tetragonal structure, it is better to say that **2** "circumvents" the oxo wall instead of breaking it. Nevertheless, complex **2** is therefore part of a small and elite group of authentic Co(IV)-oxo complexes, and in fact, is probably the best characterized example for such a species to this date. A second important issue with late transition metal-oxo complexes is the potential for bond inversion of the metal-O interactions, especially the π-bonds. The metal-O σ-bond, using a coordinate system where the metal-O vector is roughly associated with the z-axis, is mediated by the d_{z2} orbital, which also shows σ-interactions with other ligands in a given complex (especially a ligand bound trans to the oxo group). These additional interactions usually push the d_{z2} orbital to higher energy, and thus, a bond inversion is generally not expected for the metal-O σ-bond. Accordingly, the d_{z2} orbital of **2** shows about 15 – 20% O(p_z) character (from the DFT calculations). On the other hand, the Co-O π-bonds in **2** show a very interesting dichotomy that relates back to the presence of the key Co=O---HN hydrogen bond, which is oriented along the x-axis in our coordinate system (see Scheme 2). Here, the proton participating in the hydrogen bond interacts exclusively with the O(p_x) orbital, lowering this orbital in energy below the Co(d) manifold, leading to a "regular" Co-O π_x-bond, where the d_{xz} orbital of Co has about 35% O(p_x) contribution, corresponding to a very covalent interaction. The O(p_y) orbital, which lacks the hydrogen bond, shows bond inversion, where the bonding MO now has predominant metal(d) character, and the antibonding MO shows a larger O(p) admixture. In the case of **2**, the antibonding orbital shows 55 – 60% O(p_y) character, as predicted by the DFT calculations. So, although the d_{yz}/O(p_y) interaction is inverted, we are still in the regime of maximum covalency, thus limiting the amount of oxyl character associated with the oxo ligand of **2**. As a result of all of the Co(IV)-oxo interactions, the calculated spin density of the

oxo group is about 0.9 – 1.0 in **2**, which is larger compared to typical Fe(IV)-oxo complexes, supporting the partial oxyl character of the oxo group in **2**.

2 shows an electrophilic reactivity in HAT and OAT reactions. In HAT reactions, a KIE of 4.5(2) was obtained in the oxidation of xanthene and xanthene-d_2 by **2** and the dependence of the rate constant on C-H bond dissociation energy of the substrates was also observed, indicating that H-atom abstraction from the C–H bonds of substrates by **2** is the r.d.s. in the C-H bond activation reactions. In OAT reaction, a negative ρ value of –4.3 in Hammett plot and a negative slope of –15 in the plot of the rates against oxidation potentials (E_{ox}) of thioanisoles were determined in the oxidation of *para*-X-substituted thioanisoles by **2**, which indicate the electrophilic character of **2** in OAT reactions, as frequently observed in the sulfoxidation of thioanisoles by high-valent metal-oxo species.

Thus, we believe that the present study provides valuable insights into the structure and reactivity of Co-O complexes. Our findings have general implications and show how second coordination sphere interactions can tune late transition metal-oxo bonds, which are on the borderline of bond inversion. We predict that this effect has a distinct effect on reactivity, *where hydrogen bonds in fact tame highly reactive Co-oxo cores by preventing π-bond inversion*. This result therefore has general implications for late transition metal-oxo complexes, their stability and reactivity. We will conduct further studies to learn more about late transition metal-O species.

4. Experimental Section

Materials. Commercially available chemicals were purchased from Aldrich Chemical Co. and Tokyo Chemical Industry with the maximum purity available, and used as received unless otherwise indicated. Solvents, such as acetonitrile (CH_3CN), acetone, and diethyl ether (Et_2O), were dried according to published procedures and distilled under an Ar atmosphere prior to use.[73]

$H_2{}^{18}O$ (98% ^{18}O-enriched) was purchased from Berry & Associates/ICON Isotopes (Dexter, MI, USA). Iodosylbenzene (PhIO) was synthesized by a literature method,[74] and $PhI^{18}O$ was also prepared by the addition of $H_2{}^{18}O$ (5 μL) to $PhI^{16}O$ (50 μL) in trifluoroethanol (TFE) at ambient temperature, followed by waiting for 20 min for the ^{18}O-exchange to complete. $Co^{II}(OTf)_2{\cdot}2CH_3CN$ was synthesized according to a literature method.[75] The ligand, 12-TBC (= 1,4,7,10-tetrabenzyl-1,4,7,10-tetraazacyclododecane), was synthesized by a previously reported method.[76] Co^{II}(12-TBC)$(OTf)_2$ (**1**) was synthesized in a dry box: Equimolar amounts of 12-TBC (0.28 mmol, 150 mg) and $Co^{II}(CF_3SO_3)_2{\cdot}2CH_3CN$ (0.28 mmol, 120 mg) were dissolved in CH_3CN and stirred at ambient temperature for 12h in a dry box, resulting in a color change of the reaction solution to red. The resulting solution was filtered and a large volume of ether was added to the solution, giving the red precipitate of the desired product. When the red precipitate was dissolved in acetone, the color changed to purple because of the release of the coordinated acetonitrile. The purple solution in acetone was filtered and a large volume of ether was added to the solution, giving a pink precipitate. Finally, the pink precipitate was crystalized by slow diffusion of Et_2O into a saturated acetone solution of **1** at 25 ºC, giving 80% yield (185 mg). It should be noted that the spin-state of **1** in acetone is high-spin (S = 3/2), whereas in CH_3CN it is low-spin (S = 1/2).

Instrumentation. UV-vis spectra were recorded on a Hewlett Packard Agilent 8453 UV-vis spectrophotometer equipped with an UNISOKU cryostat system (USP-203; UNISOKU, Japan). The cold-spray ionization time-of-flight mass (CSI-MS) spectral data were collected on a JMS-T100CS (JEOL) mass spectrometer equipped with the CSI source [conditions: needle voltage = 2.2 kV, orifice 1 current = 50–500 nA, orifice 1 voltage = 0–20 V, ring lens voltage = 10 V, ion source temperature = 5 °C, spray temperature = –40 °C]. CSI-MS data of $[Co^{IV}(^{16}O)$(12-TBC)$]^{2+}$ (**2**-^{16}O) and $[Co^{IV}(^{18}O)$(12-TBC)$]^{2+}$ (**2**-^{18}O) were obtained by infusing the reaction solution directly into the ion source through a pre-cooled tube under high N_2 gas pressure. Resonance Raman (rRaman) scattering was dispersed by a single polychromator (Ritsu Oyo Kogaku, MC-100DG)

and detected by a liquid-nitrogen-cooled CCD detector (HORIBA JOBIN YVON, Symphony 1,024*128 Cryogenic Front Illuminated CCD Detector). Raman spectral data in Figure 4 were collected in backscattering geometry at an excitation wavelength (λ_{ex}) of 442 nm, using a spinning sample cell (NMR tube (5 mm OD)), which was placed in a thermostated quartz Dewar at -45 °C (cooled by flashing with cold N_2 gas). The laser power at the measuring point in front of the quartz Dewar was adjusted to 20 mW. rRaman spectra in Figure S3 – S5 were collected with the UniDRON (UniNanoTech, Korea) Microscope Raman chamber with 20x long working objective lens and Kymera328i-A Raman spectrometer in combination with the DR316-LDC-DD (ANDOR, UK) TE cooled CCD detector, cooled to -55 °C. The He-Cd laser (442 nm He-Cd laser set, Kimmon Koha, Japan) beams at the wavelength of 441.5 nm was used as the light source. The laser beam was focused using an objective lens with a magnifying power of 10. The solution sample in UV-vis cell (path length 0.2mm) was located into a UNISOKU Scientific Instruments (CoolSpeK UV USP-203-B, UNISOKU, Japan) for low-temperature experiments with LN_2 and N_2 gas flow. Raman shifts were calibrated using indene (accurate to within ±1 cm^{-1}). Compared the $[Co(O)(12\text{-}TBC)]^{2+}$ spectra under the same reaction conditions at Hyogo University and Ewha Womans University, the doublet frequency for Co-O stretching were obtained identically. Low-temperature EPR spectra were recorded at 5 K using an X-band Bruker EMX-plus spectrometer equipped with a dual mode cavity (ER 4116DM) [Experimental parameters as follow: microwave frequency = 9.646 GHz, microwave power = 1.0 mW, modulation amplitude = 10 G, gain = 1×10^4, modulation frequency = 100 kHz, time constant = 40.96 ms, conversion time = 81.00 ms]. Low temperatures for EPR measurements were achieved by using an Oxford Instruments ESR900 liquid He quartz cryostat with an Oxford Instruments ITC503 temperature and gas flow controller. The MCD setup employs an Oxford SM4000 cryostat and a JASCO J-815 CD spectrometer. The SM4000 cryostat consists of a liquid helium-cooled superconducting magnet providing horizontal magnetic fields of 0 – 7 T. The J-815 spectrometer uses a gaseous nitrogen-

cooled xenon lamp and a detector system consisting of two interchangeable photomultiplier tubes in the UV-vis and NIR range. The samples were loaded into a 1.5 – 300 K variable temperature insert (VTI), which offers optical access to the sample via four optical windows made from Suprasil B quartz. The spectra were recorded at different temperatures (2, 4, 8, 12, 20, and 50 K) and magnetic fields (0 – 7 T). Experiments were conducted by varying the magnetic field at the respective temperatures. Gaussian fitting of the UV-vis and MCD spectra was carried out using the program PeakFit (version 4.12). The smallest number of Gaussian functions necessary to fit the data was used for the analysis, and the quality of the fits was accessed by χ^2.

Generation and Characterization of Co^{IV}-O Species. The brown intermediate, $[Co^{IV}(O)(12\text{-}TBC)]^{2+}$ (**2**), was generated by reacting $Co^{II}(12\text{-}TBC)(CF_3SO_3)_2$ (**1**) with PhIO (3.5 equiv.; dissolved in trifluoroethanol (TFE)) in acetone/TFE (*v/v* = 4:1) at –40 °C. The full formation of **2** was confirmed by monitoring UV-vis spectral changes as evidenced by the appearance of a characteristic band at 720 nm. Similarly, the ^{18}O-labeled complex, $[Co^{IV}(^{18}O)(12\text{-}TBC)]^{2+}$ (**2**-^{18}O), was generated by using $PhI^{18}O$, which was prepared by mixing $PhI^{16}O$ (dissolved in TFE) with $H_2{}^{18}O$ (5 μL). For solution rRaman measurements, 6.0 mM solutions of $[Co^{IV}(O)(12\text{-}TBC)]^{2+}$ (**2**-^{16}O) and $[Co^{IV}(^{18}O)(12\text{-}TBC)]^{2+}$ (**2**-^{18}O) were prepared by the same method described above.

X-ray Structural Analysis. The purple rhombic single crystals of $[Co^{II}(12\text{-}TBC)(CF_3SO_3)_2]\cdot 2CH_3COCH_3$ (**1**) were grown by the slow diffusion of Et_2O into a saturated acetone solution of **1**. The crystals were mounted on a glass fiber tip with epoxy cement. Crystallographic diffraction data for **1** were collected at 100 K on a Bruker SMART AXS diffractometer equipped with a monochromator using a Mo Kα (λ = 0.71073 Å) incident beam. The CCD data were integrated and scaled using the Bruker-SAINT software package, and the structure was solved and refined using SHELXTL V 6.12.5.[77] The crystallographic data for **1** are listed in Table S1, and Table S2 lists the selected bond distances and angles. The X–ray crystallographic coordinates for structures reported here have been deposited at the Cambridge

Crystallographic Data Centre (CCDC) with the deposition number CCDC-1986346. These data can be obtained free of charge via www.ccdc.cam.ac.uk/data_request/cif (or from the Cambridge Crystallographic Data Centre, 12, Union Road, Cambridge CB2 1EZ, UK; fax:(+44) 1223-336-033; or email deposit@ccdc.cam.ac.uk).

Cobalt K-edge X-ray Absorption Spectroscopy. Acetone/TFE (*v/v* = 4:1) solutions of **1** and **2** (2.0 mM) were injected into aluminum sample holders at low temperatures between Kapton tape windows and quickly frozen in liquid nitrogen. All data were recorded at the Canadian Light Source (Saskatoon, Saskatchewan, CA) on beamline 07ID-2 (BioXAS-Spectroscopy) at 20 K with temperatures maintained using an Oxford liquid He cryostat. Light was monochromatized using a Si(220) double crystal monochromator, which was detuned 50% for harmonic rejection, and focused using a Rh mirror. Spectra were obtained in fluorescence mode using a 32 element solid-state Ge detector (Canberra) with a 3 micron cobalt filter placed between the sample and detector. Spectra were calibrated against the first inflection point of Co-foil, which was simultaneously recorded with the metallopeptide data (7709 eV). Data were obtained in 10 eV steps in the pre-edge region (7508 – 7700 eV, 1 s integration time), 0.3 eV steps in the pre-edge region (7700 – 7725 eV, 2 s integration time), 1.0 eV steps in the edge region (7725 – 7755 eV, 2 s integration time), 2.0 eV steps in the near edge region (7755 – 8000 eV, 3 s integration time), and 0.05 k steps in the far edge region (8000 eV – 16.0 $Å^{-1}$, 3 s integration time). To avoid sample photoreduction the 1 × 1 mm beam spot was moved after every 2 scans. Total fluorescence counts were maintained under 30 kHz, and a deadtime correction yielded no appreciable change to the data. The reported spectra represent the averaged spectra from 6 individual data sets. Prior to data averaging each spectrum and detector channel was individually inspected for data quality. Although data were recorded to 16 $Å^{-1}$, the data were analyzed only to 14.5 $Å^{-1}$ owing to noise at high *k*. Data were subsequently processed and analyzed as previously reported using *EXAFS123* and FEFF 9.4.[78] Errors to the models are reported as ε^2 values.

Electronic Structure Calculations. Gaussian 09[79] was used to carry out the majority of the geometry optimizations and frequency calculations performed here. The ORCA program version 4.0[80] was used to perform geometry optimizations (and following frequency calculations) in an acetone solvent field. The functionals B3LYP[81-83] and PBE0,[84] and the TZVP[85, 86] basis set were used for all geometry optimizations. ORCA 4.0 was further used to perform time-dependent DFT calculations, using a variety of functionals including BP86,[81, 87] B3LYP, PBE0 and TPSS,[88] combined with the TZVP basis set, in an acetone solvent field. In addition, the EPR and zero-field splitting parameters were calculated with ORCA using B3LYP/TZVP and PBE0/TZVP on the corresponding optimized structures obtained with the same methods. Cobalt K-edge X-ray absorption spectra were calculated using ORCA version 4.2.0 using the PBE0 hybrid functional, the def2-TZVP(-f) basis set, the ZORA relativistic approximation, and an acetone solvent field. The first 30 lowest-energy transitions were calculated for each spectrum. The spectral line-shapes were simulated by applying a 257.1 eV blue-shift and Gaussian line shape (1.3 eV peak width) to each individual transition, and summing the individual Gaussians. ORCA version 4.2.1 was used to perform the N-electron valence state perturbation theory (NEVPT2) calculations employing the def2-TZVPP basis set. Natural orbitals from an initial MP2 calculation were used as guess orbitals. The NEVPT2 calculation utilized a CAS-SCF(15,11) active space, the DLPNO variant of the fully internally contracted NEVPT2 method, and the RI approximation (def2/JK auxiliary basis set).

Conflicts of interest

There are no conflicts to declare.

Associated Content

Supporting Information Available: Structural characterization of complex **1**, additional spectroscopic characterization of complexes **1** and **2**, coordinates of DFT optimized structures, tables of DFT-calculated properties, alternative fits to the EXAFS data of **2**.

Author Information

Corresponding Authors:

jshearer@trinity.edu
lehnertn@umich.edu
wwnam@ewha.ac.kr

ORCID:

Jindou Yang: 0000-0003-2146-3808
Hai T. Dong: 0000-0002-8914-3045
Mi Sook Seo: 0000-0003-3302-2508
Virginia A. Larson: 0000-0002-7094-6286
Yong-Min Lee: 0000-0002-5553-1453
Jason Shearer: 0000-0001-7469-7304
Nicolai Lehnert: 0000-0002-5221-5498
Wonwoo Nam: 0000-0001-8592-4867

Author Contributions

† J.Y. and H.T.D. are co-first authors.

Acknowledgements

This work was supported by a grant from the National Science Foundation (CHE-1900380 to N.L. and J.S.). This work was also supported by the NRF of Korea through CRI (NRF-2021R1A3B1076539 to W.N.) and Basic Science Research Program (NRF-2020R1I1A1A01074630 to Y.-M.L. and NRF-2019R1I1A1A01055822 to M.S.S.). H.T.D. acknowledges support from an Eastman Research Fellowship. We thank Professor Kiyoung Park

and Mr. Woo Yeol Ryu (Korea Advanced Institute of Science and Technology (KAIST), Korea) for collecting NIR absorption spectra of complex **2**.

References

1. Borovik, A. S. Role of Metal-Oxo Complexes in the Cleavage of C-H Bonds. *Chem. Soc. Rev.* **2011**, *40* (4), 1870-1874.
2. Gunay, A.; Theopold, K. H. C-H Bond Activation by Metal-Oxo Compounds. *Chem. Rev.* **2010**, *110* (2), 1060-1081.
3. Guo, M.; Corona, T.; Ray, K.; Nam, W. Heme and Nonheme High-Valent Iron and Manganese Oxo Cores in Biological and Abiological Oxidation Reactions. *ACS Cent. Sci.* **2019**, *5* (1), 13-28.
4. Chen, Z.; Yin, G. The Reactivity of the Active Metal Oxo and Hydroxo Intermediates and their Implications in Oxidations. *Chem. Soc. Rev.* **2015**, *44* (5), 1083-1100.
5. Betley, T. A.; Wu, Q.; Van Voorhis, T.; Nocera, D. G. Electronic Design Criteria for O−O Bond Formation via Metal−Oxo Complexes. *Inorg. Chem.* **2008**, *47* (6), 1849-1861.
6. McEvoy, J. P.; Brudvig, G. W. Water-Splitting Chemistry of Photosystem II. *Chem. Rev.* **2006**, *106* (11), 4455-4483.
7. Fukuzumi, S.; Lee, Y.-M.; Nam, W. Acid Catalysis via Acid-Promoted Electron Transfer. *Bull. Korean Chem. Soc.* **2020**, *41* (12), 1217-1232.
8. Bollinger, J. M.; Krebs, C. Enzymatic C–H Activation by Metal–Superoxo Intermediates. *Curr. Opin. Chem. Biol.* **2007**, *11* (2), 151-158.
9. Hohenberger, J.; Ray, K.; Meyer, K. The Biology and Chemistry of High-Valent Iron–Oxo and Iron–Nitrido Complexes. *Nat. Commun.* **2012**, *3* (1), 720-720.
10. Engelmann, X.; Monte-Pérez, I.; Ray, K. Oxidation Reactions with Bioinspired Mononuclear Non-Heme Metal-Oxo Complexes. *Angew. Chem., Int. Ed.* **2016**, *55* (27), 7632-7649.
11. Ray, K.; Pfaff, F. F.; Wang, B.; Nam, W. Status of Reactive Non-Heme Metal-Oxygen Intermediates in Chemical and Enzymatic Reactions. *J. Am. Chem. Soc.* **2014**, *136* (40), 13942-13958.
12. Cox, N.; Pantazis, D. A.; Neese, F.; Lubitz, W. Biological Water Oxidation. *Acc. Chem. Res.* **2013**, *46* (7), 1588-1596.
13. Pantazis, D. A.; Orio, M.; Petrenko, T.; Zein, S.; Lubitz, W.; Messinger, J.; Neese, F. Structure of the Oxygen-Evolving Complex of Photosystem II: Information on the S_2 State through Quantum Chemical Calculation of its Magnetic Properties. *Phys. Chem. Chem. Phys.* **2009**, *11* (31), 6788-6798.
14. Cox, N.; Retegan, M.; Neese, F.; Pantazis, D. A.; Boussac, A.; Lubitz, W. Photosynthesis. Electronic Structure of the Oxygen-Evolving Complex in Photosystem II Prior to O-O Bond Formation. *Science* **2014**, *345* (6198), 804-808.
15. Kundu, S.; Schwalbe, M.; Ray, K. Metal-Oxo-Mediated O-O Bond Formation Reactions in Chemistry and Biology. *BioInorg. React. Mech.* **2012**, *8* (1-2), 41-57.
16. Yocum, C. F. The Calcium and Chloride Requirements of the O_2 Evolving Complex. *Coord. Chem. Rev.* **2008**, *252* (3-4), 296-305.
17. Poulos, T. L. Heme Enzyme Structure and Function. *Chem. Rev.* **2014**, *114* (7), 3919-3962.
18. Huang, X.; Groves, J. T. Oxygen Activation and Radical Transformations in Heme Proteins and Metalloporphyrins. *Chem. Rev.* **2018**, *118* (5), 2491-2553.

19. Nam, W.; Lee, Y.-M.; Fukuzumi, S. Tuning Reactivity and Mechanism in Oxidation Reactions by Mononuclear Nonheme Iron(IV)-Oxo Complexes. *Acc. Chem. Res.* **2014**, *47* (4), 1146-1154.
20. Nam, W. Dioxygen Activation by Metalloenzymes and Models. *Acc. Chem. Res.* **2007**, *40* (7), 465 and references therein.
21. Elwell, C. E.; Gagnon, N. L.; Neisen, B. D.; Dhar, D.; Spaeth, A. D.; Yee, G. M.; Tolman, W. B. Copper–Oxygen Complexes Revisited: Structures, Spectroscopy, and Reactivity. *Chem. Rev.* **2017**, *117* (3), 2059-2107.
22. Nam, W.; Lee, Y.-M.; Fukuzumi, S. Hydrogen Atom Transfer Reactions of Mononuclear Nonheme Metal-Oxygen Intermediates. *Acc. Chem. Res.* **2018**, *51* (9), 2014-2022.
23. Costas, M. Selective C-H Oxidation Catalyzed by Metalloporphyrins. *Coord. Chem. Rev.* **2011**, *255* (23-24), 2912-2932.
24. Zhang, M.; De Respinis, M.; Frei, H. Time-Resolved Observations of Water Oxidation Intermediates on a Cobalt Oxide Nanoparticle Catalyst. *Nat. Chem.* **2014**, *6* (4), 362-367.
25. Nocera, D. G. The Artificial Leaf. *Acc. Chem. Res.* **2012**, *45* (5), 767-776.
26. Nguyen, A. I.; Ziegler, M. S.; Oña-Burgos, P.; Sturzbecher-Hohne, M.; Kim, W.; Bellone, D. E.; Tilley, T. D. Mechanistic Investigations of Water Oxidation by a Molecular Cobalt Oxide Analogue: Evidence for a Highly Oxidized Intermediate and Exclusive Terminal Oxo Participation. *J. Am. Chem. Soc.* **2015**, *137* (40), 12865-12872.
27. Parent, A. R.; Sakai, K. Progress in Base-Metal Water Oxidation Catalysis. *ChemSusChem* **2014**, *7* (8), 2070-2080.
28. Hadt, R. G.; Hayes, D.; Brodsky, C. N.; Ullman, A. M.; Casa, D. M.; Upton, M. H.; Nocera, D. G.; Chen, L. X. X-ray Spectroscopic Characterization of Co(IV) and Metal-Metal Interactions in Co_4O_4: Electronic Structure Contributions to the Formation of High-Valent States Relevant to the Oxygen Evolution Reaction. *J. Am. Chem. Soc.* **2016**, *138* (34), 11017-11030.
29. Winkler, J. R.; Gray, H. B. Electronic Structures of Oxo-Metal Ions. *Struct. Bond.* **2012**, *142*, 17-28.
30. Larson, V.; Battistella, B.; Ray, K.; Lehnert, N.; Nam, W. Iron and Manganese Oxo Complexes, Oxo Wall and Beyond. *Nat. Chem. Rev.* **2020**, *4*, 404–419.
31. Hay-Motherwell, R. S.; Wilkinson, G.; Hussain-Bates, B.; Hursthouse, M. B. Synthesis and X-ray Crystal Structure of Oxotrimesityliridium(V). *Polyhedron* **1993**, *12* (16), 2009-2012.
32. Poverenov, E.; Efremenko, I.; Frenkel, A. I.; Ben-David, Y.; Shimon, L. J. W.; Leitus, G.; Konstantinovski, L.; Martin, J. M. L.; Milstein, D. Evidence for a Terminal Pt(IV)-Oxo Complex Exhibiting Diverse Reactivity. *Nature* **2008**, *455* (7216), 1093-1096.
33. O'Halloran, K. P.; Zhao, C.; Ando, N. S.; Schultz, A. J.; Koetzle, T. F.; Piccoli, P. M. B.; Hedman, B.; Hodgson, K. O.; Bobyr, E.; Kirk, M. L.; Knottenbelt, S.; Depperman, E. C.; Stein, B.; Anderson, T. M.; Cao, R.; Geletii, Y. V.; Hardcastle, K. I.; Musaev, D. G.; Neiwert, W. A.; Fang, X.; Morokuma, K.; Wu, S.; Kögerler, P.; Hill, C. L. Revisiting the Polyoxometalate-Based Late-Transition-Metal-Oxo Complexes: The "Oxo Wall" Stands. *Inorg. Chem.* **2012**, *51* (13), 7025-7031.
34. Goetz, M. K.; Hill, E. A.; Filatov, A. S.; Anderson, J. S. Isolation of a Terminal Co(III)-Oxo Complex. *J. Am. Chem. Soc.* **2018**, *140* (41), 13176-13180.
35. Goetz, M. K.; Anderson, J. S. Experimental Evidence for pKa‐Driven Asynchronicity in C−H Activation by a Terminal Co(III)−Oxo Complex. *J. Am. Chem. Soc.* **2019**, *141* (9), 4051–4062.
36. Nguyen, A. I.; Hadt, R. G.; Solomon, E. I.; Tilley, T. D. Efficient C–H Bond Activations via O_2 Cleavage by a Dianionic Cobalt(II) Complex. *Chem. Sci.* **2014**, *5* (7), 2874-2878.
37. Chavez, F. A.; Rowland, J. M.; Olmstead, M. M.; Mascharak, P. K. Syntheses, Structures, and Reactivities of Cobalt(III)−Alkylperoxo Complexes and Their Role in Stoichiometric and Catalytic Oxidation of Hydrocarbons. *J. Am. Chem. Soc.* **1998**, *120* (35), 9015-9027.

38. Chavez, F. A.; Mascharak, P. K. Co(III)−Alkylperoxo Complexes: Syntheses, Structure−Reactivity Correlations, and Use in the Oxidation of Hydrocarbons. *Acc. Chem. Res.* **2000**, *33* (88), 539-545.
39. Li, N.; Lu, W.; Pei, K.; Yao, Y.; Chen, W. Formation of High-Valent Cobalt-Oxo Phthalocyanine Species in a Cellulose Matrix for Eliminating Organic Pollutants. *Appl. Catal. B* **2015**, *163*, 105-112.
40. Nam, W.; Kim, I.; Kim, Y.; Kim, C. Biomimetic Alkane Hydroxylation by Cobalt(III) Porphyrin Complex and m-Chloroperbenzoic Acid. *Chem. Commun.* **2001**, 1262-1263.
41. Pfaff, F. F.; Kundu, S.; Risch, M.; Pandian, S.; Heims, F.; Pryjomska-Ray, I.; Haack, P.; Metzinger, R.; Bill, E.; Dau, H.; Comba, P.; Ray, K. An Oxocobalt(IV) Complex Stabilized by Lewis Acid Interactions with Scandium(III) Ions. *Angew. Chem., Int. Ed.* **2011**, *50* (7), 1711-1715.
42. Lacy, D. C.; Park, Y. J.; Ziller, J. W.; Yano, J.; Borovik, A. S. Assembly and Properties of Heterobimetallic $Co^{II/III}/Ca^{II}$ Complexes with Aquo and Hydroxo Ligands. *J. Am. Chem. Soc.* **2012**, *134* (42), 17526-17535.
43. Hong, S.; Pfaff, F. F.; Kwon, E.; Wang, Y.; Seo, M.-S. S.; Bill, E.; Ray, K.; Nam, W. Spectroscopic Capture and Reactivity of a Low-Spin Cobalt(IV)-Oxo Complex Stabilized by Binding Redox-Inactive Metal Ions. *Angew. Chem., Int. Ed.* **2014**, *53* (39), 10403-10407.
44. Collins, T. J.; Powell, R. D.; Slebodnick, C.; Uffelman, E. S. Stable Highly Oxidizing Cobalt Complexes of Macrocyclic Ligands. *J. Am. Chem. Soc.* **1991**, *113* (22), 8419-8425.
45. Popescu, D.-L.; Chanda, A.; Stadler, M.; de Oliveira, F. T.; Ryabov, A. D.; Münck, E.; Bominaar, E. L.; Collins, T. J. High-Valent First-Row Transition-Metal Complexes of Tetraamido (4*N*) and Diamidodialkoxido or Diamidophenolato (2*N*/2*O*) Ligands: Synthesis, Structure, and Magnetochemistry. *Coord. Chem. Rev.* **2008**, *252* (18-20), 2050-2071.
46. Das, D.; Pattanayak, S.; Singh, K. K.; Garai, B.; Sen Gupta, S. Electrocatalytic Water Oxidation by a Molecular Cobalt Complex through a High Valent Cobalt Oxo Intermediate. *Chem. Commun.* **2016**, *52* (79), 11787-11790.
47. Swart, M. A Change in the Oxidation State of Iron: Scandium Is Not Innocent. *Chem. Commun.* **2013**, *49* (59), 6650-6652.
48. Prakash, J.; Rohde, G. T.; Meier, K. K.; Jasniewski, A. J.; Van Heuvelen, K. M.; Münck, E.; Que, L., Jr. Spectroscopic Identification of an Fe^{III} Center, Not Fe^{IV}, in the Crystalline Sc−O−Fe Adduct Derived from $[Fe^{IV}(O)(TMC)]^{2+}$. *J. Am. Chem. Soc.* **2015**, *137* (10), 3478-3481.
49. Hong, S.; Lee, Y.-M.; Sankaralingam, M.; Vardhaman, A. K.; Park, Y. J.; Cho, K.-B.; Ogura, T.; Sarangi, S.; Fukuzumi, S.; Nam, W. A Manganese(V)-Oxo Complex: Synthesis by Dioxygen Activation and Enhancement of Its Oxidizing Power by Binding Scandium Ion. *J. Am. Chem. Soc.* **2016**, *138* (27), 8523-8532.
50. Wang, B.; Lee, Y.-M.; Tcho, W.-Y.; Tussupbayev, S.; Kim, S.-T.; Kim, Y.; Seo, M. S.; Cho, K.-B.; Dede, Y.; Keegan, B. C.; Ogura, T.; Kim, S. H.; Ohta, T.; Baik, M.-H.; Ray, K.; Shearer, J.; Nam, W. Synthesis and Reactivity of a Mononuclear Non-Haem Cobalt(IV)-Oxo Complex. *Nat. Commun.* **2017**, *8*, 14839.
51. Risch, M.; Khare, V.; Zaharieva, I.; Gerencser, L.; Chernev, P.; Dau, H. Cobalt-Oxo Core of a Water-Oxidizing Catalyst Film. *J. Am. Chem. Soc.* **2009**, *131* (20), 6936-6937.
52. Huck-Iriart, C.; Soler, L.; Casanovas, A.; Marini, C.; Prat, J.; Llorca, J.; Escudero, C. Unraveling the Chemical State of Cobalt in Co-Based Catalysts during Ethanol Steam Reforming: an in Situ Study by Near Ambient Pressure XPS and XANES. *ACS Catal.* **2018,** *8* (10), 9625-9636.
53. Westre, T. E.; Kennepohl, P.; DeWitt, J. G.; Hedman, B.; Hodgson, K. O.; Solomon, E. I. A Multiplet Analysis of Fe K-edge 1s->3d Pre-edge Features of Iron Complexes. *J. Am. Chem. Soc.* **1997**, *119* (27), 6297-6314.

54. Leto, D. F.; Jackson, T. A. Mn K-Edge X-ray Absorption Studies of Oxo- and Hydroxo-Manganese(IV) Complexes: Experimental and Theoretical Insights into Pre-Edge Properties. *Inorg. Chem.* **2014**, *53* (12), 6179-6194.
55. Jackson, T. A.; Rohde, J. U.; Seo, M. S.; Sastri, C. V.; DeHont, R.; Stubna, A.; Ohta, T.; Kitagawa, T.; Munck, E.; Nam, W.; Que, L. Axial Ligand Effects on the Geometric and Electronic Structures of Nonheme Oxoiron(IV) Complexes. *J. Am. Chem. Soc.* **2008**, *130* (37), 12394-12407.
56. Hong, S.; So, H.; Yoon, H.; Cho, K.-B.; Lee, Y.-M.; Fukuzumi, S.; Nam, W. Reactivity Comparison of High-Valent Iron(IV)-Oxo Complexes Bearing *N*-Tetramethylated Cyclam Ligands with Different Ring Size. *Dalton Trans.* **2013**, *42* (22), 7842-7845.
57. Sastri, C. V.; Park, M. J.; Ohta, T.; Jackson, T. A.; Stubna, A.; Seo, M. S.; Lee, J.; Kim, J.; Kitagawa, T.; Münck, E.; Que, L., Jr.; Nam, W. Axial Ligand Substituted Nonheme Fe^{IV}=O Complexes: Observation of Near-UV LMCT Bands and Fe=O Raman Vibrations. *J. Am. Chem. Soc.* **2005**, *127* (36), 12494-12495.
58. Petasis, D. T.; Hendrich, M. P. Quantitative Interpretation of Multifrequency Multimode EPR Spectra of Metal Containing Proteins, Enzymes, and Biomimetic Complexes. *Meth. Enzymol.* **2015**, *563*, 171-208.
59. Solomon, E. I.; Pavel, E. G.; Loeb, K. E.; Campochiaro, C. Magnetic Circular Dichroism Spectroscopy as a Probe of the Geometric and Electronic Structure of Non-Heme Ferrous Enzymes. *Coord. Chem. Rev.* **1995**, *144*, 369-460.
60. Lehnert, N.; DeBeer George, S.; Solomon, E. I. Recent Advances in Bioinorganic Spectroscopy. *Curr. Opin. Chem. Biol.* **2001**, *5* (2), 176-187.
61. DiMucci, I. M.; MacMillan, S. N.; Walroth, R. C.; Lancaster, K. M. Scrutinizing "Ligand Bands" via Polarized Single-Crystal X-ray Absorption Spectra of Copper(I) and Copper(II) Bis-2,2′-bipyridine Species. *Inorg. Chem.* **2020**, *59* (18), 13416-13426.
62. Carsch, K. M.; Lukens, J. T.; DiMucci, I. M.; Iovan, D. A.; Zheng, S. L.; Lancaster, K. M.; Betley, T. A. Electronic Structures and Reactivity Profiles of Aryl Nitrenoid-Bridged Dicopper Complexes. *J. Am. Chem. Soc.* **2020**, *142* (5), 2264-2276.
63. Kal, S.; Xu, S. N.; Que, L. R. Bio-Inspired Nonheme Iron Oxidation Catalysis: Involvement of Oxoiron(V) Oxidants in Cleaving Strong C-H Bonds. *Angew. Chem., Int. Ed.* **2020**, *59* (19), 7332-7349.
64. Kisgeropoulos, E. C.; Manesis, A. C.; Shafaat, H. S. Ligand Field Inversion as a Mechanism to Gate Bioorganometallic Reactivity: Investigating a Biochemical Model of Acetyl CoA Synthase Using Spectroscopy and Computation. *J. Am. Chem. Soc.* **2021**, *143* (2), 849-867.
65. Hong, S.; Wang, B.; Seo, M. S.; Lee, Y.-M.; Kim, M. J.; Kim, H. R.; Ogura, T.; Garcia-Serres, R.; Clemancey, M.; Latour, J. M.; Nam, W. Highly Reactive Nonheme Iron(III) Iodosylarene Complexes in Alkane Hydroxylation and Sulfoxidation Reactions. *Angew. Chem., Int. Ed.* **2014**, *53* (25), 6388-6392.
66. Arias, J.; Newlands, C. R.; Abu-Omar, M. M. Kinetics and Mechanisms of Catalytic Oxygen Atom Transfer with Oxorhenium(V) Oxazoline Complexes. *Inorg. Chem.* **2001**, *40* (9), 2185-2192.
67. Taki, M.; Itoh, S.; Fukuzumi, S. Oxo-Transfer Reaction from a Bis(μ-oxo)dicopper(III) Complex to Sulfides. *J. Am. Chem. Soc.* **2002**, *124* (6), 998-1002.
68. McPherson, L. D.; Drees, M.; Khan, S. I.; Strassner, T.; Abu-Omar, M. M. Multielectron Atom Transfer Reactions of Perchlorate and Other Substrates Catalyzed by Rhenium Oxazoline and Thiazoline Complexes: Reaction Kinetics, Mechanisms, and Density Functional Theory Calculations. *Inorg. Chem.* **2004**, *43* (13), 4036-4050.

69. Cho, J.; Woo, J.; Nam, W. An "End-On" Chromium(III)-Superoxo Complex: Crystallographic and Spectroscopic Characterization and Reactivity in C-H Bond Activation of Hydrocarbons. *J. Am. Chem. Soc.* **2010**, *132* (17), 5958-5959.
70. Kim, Y. M.; Cho, K.-B.; Cho, J.; Wang, B. J.; Li, C. S.; Shaik, S.; Nam, W. A Mononuclear Non-Heme High-Spin Iron(III)-Hydroperoxo Complex as an Active Oxidant in Sulfoxidation Reactions. *J. Am. Chem. Soc.* **2013**, *135* (24), 8838-8841.
71. Hong, S.; Lu, X. Y.; Lee, Y.-M.; Seo, M. S.; Ohta, T.; Ogura, T.; Clemancey, M.; Maldivi, P.; Latour, J. M.; Sarangi, R.; Nam, W. Achieving One-Electron Oxidation of a Mononuclear Nonheme Iron(V)-Imido Complex. *J. Am. Chem. Soc.* **2017**, *139* (41), 14372-14375.
72. Ray, K.; Heims, F.; Pfaff, F. F. Terminal Oxo and Imido Transition-Metal Complexes of Groups 9–11. *Eur. J. Inorg. Chem.* **2013**, *2013* (22-23), 3784-3807.
73. Armarego, W. L. F.; Chai, C. *Purification of Laboratory Chemicals*. 6 ed.; Pergamon Press: Oxford: 2009.
74. Saltzman, H.; Sharefkin, J. G. Organic Syntheses. Collective ed.; Wiley: New York, 1973; pp 658-659.
75. Dixon, N. E.; Lawrance, G. A.; Lay, P. A.; Sargeson, A. M.; Taube, H. Trifluoromethanesulfonates and Trifluoromethanesulfonato-*O* Complexes. Angelici, R. J., Ed. John Wiley & Sons, Ltd: 1990; Vol. 28, pp 70-76.
76. Counsell, A. J.; Jones, A. T.; Todd, M. H.; Rutledge, P. J. A Direct Method for the *N*-Tetraalkylation of Azamacrocycles. *Beilstein J. Org. Chem.* **2016**, *12* (1), 2457-2461.
77. Sheldrick, G. M. *SHELXTL/PC Version 6.12 for Windows XP*, Bruker AXS Inc.: Madison, Wisconsin, USA, 2001.
78. Yang, J.; Seo, M. S.; Kim, K. H.; Lee, Y.-M.; Fukuzumi, S.; Shearer, J.; Nam, W. Structure and Unprecedented Reactivity of a Mononuclear Nonheme Cobalt(III) Iodosylbenzene Complex. *Angew. Chem., Int. Ed.* **2020**, *59* (32), 13581-13585.
79. Frisch, M. J.; Trucks, G. W.; Schlegel, H. B.; Scuseria, G. E.; Robb, M. A.; Cheeseman, J. R.; Scalmani, G.; Barone, V.; Mennucci, B.; Petersson, G. A.; Nakatsuji, H.; Caricato, M.; Li, X.; Hratchian, H. P.; Izmaylov, A. F.; Bloino, J.; Zheng, G.; Sonnenberg, J. L.; Hada, M.; Ehara, M.; Toyota, K.; Fukuda, R.; Hasegawa, J.; Ishida, M.; Nakajima, T.; Honda, Y.; Kitao, O.; Nakai, H.; Vreven, T.; Montgomery, J. A. Jr.; Peralta, J. E.; Ogliaro, F.; Bearpark, M.; Heyd, J. J.; Brothers, E.; Kudin, K. N.; Staroverov, V. N.; Kobayashi, R.; Normand, J.; Raghavachari, K.; Rendell, A.; Burant, J. C.; Iyengar, S. S.; Tomasi, J.; Cossi, M.; Rega, N.; Millam, J. M.; Klene, M.; Knox, J. E.; Cross, J. B.; Bakken, V.; Adamo, C.; Jaramillo, J.; Gomperts, R.; Stratmann, R. E.; Yazyev, O.; Austin, A. J.; Cammi, R.; Pomelli, C.; Ochterski, J. W.; Martin, R. L.; Morokuma, K.; Zakrzewski, V. G.; Voth, G. A.; Salvador, P.; Dannenberg, J. J.; Dapprich, S.; Daniels, A. D.; Farkas, O.; Foresman, J. B.; Ortiz, J. V.; Cioslowski, J.; Fox, D. J. *Gaussian 09*, Gaussian, Inc.: Wallingford CT, 2009.
80. Neese, F. Software Update: the ORCA Program System, Version 4.0. *Wiley Interdisciplinary Reviews-Computational Molecular Science* **2018**, *8* (1).
81. Becke, A. D. Density-Functional Exchange-Energy Approximation with Correct Asymptotic-Behavior. *Phys. Rev. A* **1988**, *38* (6), 3098-3100.
82. Becke, A. D. Density-Functional Thermochemistry. III. The Role of Exact Exchange. *J. Chem. Phys.* **1993**, *98* (7), 5648-5652.
83. Lee, C.; Yang, W.; Parr, R. G. Development of the Colle-Salvetti Correlation-Energy Formula into a Functional of the Eelectron Density. *Phys. Rev. B* **1988**, *37* (2), 785 - 789.
84. Adamo, C.; Barone, V. Toward Reliable Density Functional Methods without Adjustable Parameters: The PBE0 model. *J. Chem. Phys.* **1999**, *110* (13), 6158-6170.
85. Weigend, F. Accurate Coulomb-Fitting Basis Sets for H to Rn. *Phys. Chem. Chem. Phys.* **2006**, *8* (9), 1057-1065.

86. Weigend, F.; Ahlrichs, R. Balanced Basis Sets of Split Valence, Triple Zeta Valence and Quadruple Zeta Valence Quality for H to Rn: Design and Assessment of Accuracy. *Phys. Chem. Chem. Phys.* **2005**, *7* (18), 3297-3305.
87. Perdew, J. P. Density-Functional Approximation for the Correlation-Energy of the Inhomogeneous Electron-Gas. *Phys. Rev. B* **1986**, *33* (12), 8822-8824.
88. Tao, J. M.; Perdew, J. P.; Staroverov, V. N.; Scuseria, G. E. Climbing the Density Functional Ladder: Nonempirical Meta-Generalized Gradient Approximation Designed for Molecules and Solids. *Phys. Rev. Lett.* **2003**, *91* (14), 146401-146404.

Table of Contents